

1 **Dynamically Downscaled Future Projections of the Northwest Atlantic Ocean**  
2 **Across Low to High Emissions Scenarios**

3  
4 Dongmin Kim<sup>1,2</sup>, Andrew C. Ross<sup>3</sup>, Sang-Ik Shin<sup>4,5</sup>, Fabian A. Gomez<sup>6,2</sup>, Jasmin G. John<sup>2</sup>,  
5 Denis L. Volkov<sup>1,2</sup>, Sang-Ki Lee<sup>2</sup>, Michael A. Alexander<sup>7</sup> and Charles A. Stock<sup>3</sup>

6  
7 <sup>1</sup>Cooperative Institute for Marine and Atmospheric Studies, University of Miami, Miami, FL,  
8 USA

9 <sup>2</sup>NOAA/OAR/Atlantic Oceanographic & Meteorological Laboratory, Miami, FL, USA

10 <sup>3</sup>NOAA/OAR/Geophysical Fluid Dynamics Laboratory, Princeton, NJ, USA,

11 <sup>4</sup>Cooperative Institute for Research in Environmental Sciences, University of Colorado Boulder,  
12 Boulder, CO, USA,

13 <sup>5</sup>NOAA/OAR/Physical Sciences Laboratory, Boulder, CO, USA,

14 <sup>6</sup>Northern Gulf Institute, Mississippi State University, Starkville, MS, USA

15 <sup>7</sup>Department of Atmospheric and Oceanic Sciences, University of Colorado Boulder, Boulder,  
16 CO, USA

17  
18  
19  
20 **Corresponding author:** Dr. Dongmin Kim ([dongmin.kim@noaa.gov](mailto:dongmin.kim@noaa.gov)), Cooperative Institute for  
21 Marine and Atmospheric Studies, University of Miami, 4600 Rickenbacker Causeway, Miami, FL  
22 33149, USA.

24 **Abstract**

25 We used a high-resolution (1/12°) Modular Ocean Model version 6 implementation for the  
26 the Northwest Atlantic Ocean (MOM6-NWA12) to dynamically downscale Geophysical Fluid  
27 Dynamics Laboratory Earth System Model version 4.1 (GFDL-ESM4.1) projections for the 21st  
28 century. Simulations were conducted under four different Coupled Model Intercomparison  
29 Project Phase 6 emission scenarios. MOM6-NWA12 accurately simulates the spatial patterns of  
30 sea surface temperature, salinity, and dynamic sea surface height (SSH) during the historical  
31 period. In particular, the Gulf Stream's strength, position, recirculation, and separation from the  
32 U.S. East Coast are significantly improved in MOM6-NWA12 compared to the coarse-resolution  
33 GFDL-ESM4.1. Projected end-of-century warming varied strongly between scenarios, from ~  
34 4 °C under prior "worst case" emissions scenarios (SSP-585), 2~3 °C under intermediate  
35 scenarios (SSP-245, SSP-370) more consistent with current trajectories, to ~ 1 °C under  
36 aggressive mitigation (SSP-126). Consistent with a significant weakening of the Atlantic  
37 Meridional Overturning Circulation projected by GFDL-ESM4.1, MOM6-NWA12 shows a  
38 substantial volume transport reduction in the Western Boundary Current (WBC) system (i.e.,  
39 Yucatan Current, Florida Current, Antilles Current, and the Deep Western Boundary Current)  
40 toward the late 21st century (between 23 and 38 %, varying by scenario). This projected  
41 weakening of the WBC system and the associated reduction in the coastal upwelling of cold,  
42 fresh subsurface waters lead to a significant increase in ocean temperature, salinity, and dynamic  
43 SSH along the U.S. southeast and northeast Coasts, particularly in the South Atlantic Bight.

44

45 **1. Introduction**

46 The Northwest Atlantic Ocean (NWA), including the United States (US) East and Gulf  
47 Coasts, and the Caribbean Sea, is characterized by large spatial heterogeneity in ocean conditions  
48 and complex interactions between ocean circulation and biogeochemistry (e.g., Wang et al.,  
49 2013; Muller-Karger et al., 2015; Wanninkhof et al., 2015; Gomez et al., 2020; 2022; Friedrichs  
50 et al., 2019; Zhang et al., 2023). A myriad of living marine resources inhabit this region,  
51 including the South Florida coral reefs, lobsters and shellfish, demersal fish species like  
52 groupers, snappers, cod and haddock, and migratory pelagic fish species like bluefin tuna and  
53 king mackerel, all of whose distribution and abundance are influenced by changes in ocean  
54 temperature and circulation (e.g., Weinberg 2005; Bell et al., 2015; Karnauskas et al., 2013,  
55 2015; Tanaka et al., 2020). Previous studies have shown that portions of the ocean ecosystem are  
56 modulated by large scale climate variability, such as El Niño Southern Oscillation and Atlantic  
57 Multidecadal Oscillation, through associated changes in ocean circulation and river runoff (e.g.,  
58 Alexander and Scott, 2008; Gomez et al., 2019, 2024). Moreover, the region is undergoing  
59 sustained warming, particularly along the US South and East Coasts, where the surface  
60 temperature warming rate was about two or three times faster than that of the global ocean  
61 average for 1970-2020 (e.g., Pershing et al., 2015; Wang et al., 2023).

62 Previous studies have also attributed regional acceleration and spatial variation of the US  
63 East Coast sea level rise to ocean circulation changes, including a weakening of the Gulf Stream  
64 (e.g., Ezer et al., 2013; Ezer, 2015; Goddard et al., 2015; Park and Sweet, 2015; Dong et al.,  
65 2019), warming of the Gulf Stream and the entire subtropical gyre (e.g., Domingues et al., 2018;  
66 Volkov et al., 2019, 2023; Steinberg et al., 2024; Huang et al., 2025), and a slowdown of the  
67 Atlantic Meridional Overturning Circulation (AMOC, e.g., Levermann et al., 2005; Little et al.,  
68 2017, 2019). While progress has been made in understanding ocean conditions off the US East

69 and Gulf Coasts and in the Caribbean Sea, substantial uncertainties still remain regarding future  
70 changes in regional ocean circulation and their sensitivity to greenhouse gas emissions scenarios.  
71 Consequently, it is essential to investigate projected changes in ocean circulation across  
72 scenarios to improve our understanding of future ocean conditions and ecosystem dynamics  
73 across the Northwest Atlantic.

74 Global models, such as General Circulation models (GCMs) and Earth System Models  
75 (ESMs), offer valuable insights into future ocean conditions under various climate scenarios.  
76 However, they are often limited in spatial resolution due to computational constraints and may  
77 face significant uncertainties due to limitations in representing the fine-scale ocean circulation  
78 and thermohaline structures, particularly in coastal regions. Hence, high-resolution, eddy-  
79 resolving ocean models are critical for addressing these limitations, providing improved  
80 representations of historical ocean circulation across multiple timescales and offering more  
81 reliable future projections (e.g., Drenkard et al., 2021). To leverage the benefits of resolving  
82 eddies and shelf-scale circulation while lowering the computational burden, multiple studies  
83 have applied dynamic downscaling techniques to better understand and project regional impacts  
84 of climate change on NWA ocean systems (e.g., Liu et al., 2012, 2015; Alexander et al., 2020;  
85 Shin and Alexander, 2020; Rutherford et al., 2024).

86 By refining the outputs of GCMs/ESMs using high-resolution regional models, dynamical  
87 downscaling can capture finer-scale processes and interactions that are often missed by coarse-  
88 resolution models. For example, the projected weakening of the Loop Current and associated  
89 reduction in warm water transport through the Yucatan Channel are poorly resolved in Coupled  
90 Model Intercomparison Project Phase 5 (CMIP5) and CMIP6 global models, leading to an  
91 overestimation of SST warming over the northern part of the Gulf of America (GoA; a.k.a. Gulf

92 of Mexico) and underestimation of SST warming along the West Florida shelf - an issue better  
93 addressed by high-resolution downscaled models (e.g., Liu et al., 2012, 2015). Similarly,  
94 systematic CMIP model biases in the Gulf Stream representation led to under-estimation of  
95 warming of Northeast U.S. waters associated with future changes in the Gulf Stream path (Saba  
96 et al., 2016).

97 In line with these efforts, the National Oceanic and Atmospheric Administration (NOAA)  
98 Changing Ecosystems and Fisheries Initiative (CEFI) modeling team has developed a high-  
99 resolution regional ocean model - the Modular Ocean Model version 6 at  $1/12^\circ$  horizontal  
100 resolution ( $\sim 8$  km) for the Northwest Atlantic Ocean (MOM6-NWA12; Ross et al., 2023).  
101 MOM6-NWA12 is configured to capture key regional features and simulate ocean dynamics in  
102 the Northwest Atlantic with high fidelity. This model provides a valuable framework for  
103 studying the complex interactions between large-scale processes and local features that govern  
104 both physical and biogeochemical variability in the region. MOM6-NWA12 demonstrates strong  
105 performance in reproducing a broad range of observed physical and biogeochemical conditions  
106 during the hindcast period (1993-2020, Ross et al., 2023). Furthermore, it exhibits skillful  
107 seasonal to decadal forecast capabilities for SST anomalies (SSTAs, Koul et al., 2024; Ross et  
108 al., 2024). However, while MOM6-NWA12 has shown promise for seasonal and decadal  
109 predictions, its potential for multi-decadal (30~100 years) projections remains unexplored.

110 In this study, we use the high-resolution MOM6-NWA12 model to dynamically downscale  
111 future projections from the Geophysical Fluid Dynamics Laboratory's Earth System Model  
112 version 4.1 (GFDL-ESM4.1) for the Northwest Atlantic Ocean. With this downscaling  
113 procedure, we aim to generate more accurate and regionally relevant projections of future ocean  
114 conditions. Unlike prior studies, which used a single greenhouse gas emissions scenario, we

115 consider the range of potential ocean futures from projections using four different scenarios (i.e.,  
116 Shared Socioeconomic Pathways; SSP-126, SSP-245, SSP-375, and SSP-585) spanning  
117 aggressive mitigation to high emissions pathways beyond our current trajectory. This allows us  
118 to identify the NWA responses to future climate change that are sensitive to emissions pathways  
119 from those that are not, and to explore mechanisms underlying these contrasts. We also build on  
120 prior work to understand regional hot-spots of ocean change and their drivers. This approach  
121 enhances our understanding of regional ocean dynamics and supports the development of  
122 effective mitigation and adaptation strategies in response to climate change.

123

## 124 **2. Model and downscaling settings**

### 125 2.1 MOM6-NWA12

126 MOM6-COBALT-NWA12 is a coupled ocean circulation and sea ice model which can also  
127 include coupled ocean biogeochemistry (Ross et al., 2023). Here, we consider a “physics-only”  
128 implementation of this system (i.e., MOM6-NWA12), which has also been applied for seasonal  
129 and decadal prediction applications (Ross et al., 2024; Koul et al., 2024). The model spans the  
130 Northwest Atlantic Ocean, including the Caribbean Sea, the Gulf Coast, and the U.S. East Coast  
131  $98^{\circ}\text{W}$ - $36^{\circ}\text{W}$  and  $5^{\circ}\text{N}$ - $52^{\circ}\text{N}$ , and has  $775 \times 845$  grid points (Fig. 1). The nominal horizontal  
132 resolution is about  $1/12^{\circ}$ . The zonal distance between grid points varies with latitude, from  $\sim 9$   
133 km at the southern boundary to  $\sim 5$  km at the northern boundary. The model has 75 vertical  
134 layers using a  $z^*$ -coordinate, a depth coordinate rescaled with the free surface (Adcroft and  
135 Campin, 2004). The vertical resolution is finest near the surface, where the layer thickness is 2  
136 m, increasing gradually with depth to a maximum thickness of 250 m above the deepest model  
137 depth of 6500 m. The model’s subgrid-scale parameterizations are adapted from the  $1/4^{\circ}$  global

138 MOM6, with updates and modifications to account for the increased horizontal resolution (Ross  
139 et al., 2023). MOM6-NWA12 has the option of using time steps for thermodynamics and ocean-  
140 biogeochemistry longer than the baroclinic time step, which significantly reduces the running  
141 time for coupled model simulations. More detailed model description, additional features, and  
142 parameterization settings can be found in Ross et al. (2023).

143

## 144 2.2 GFDL-ESM4.1

145 NOAA GFDL's Earth System Model version 4.1 (GFDL-ESM4.1, Dunne et al. 2020)  
146 provides the boundary conditions for the MOM6-NWA12 simulations. We carried out four sets  
147 of MOM6-NWA12 simulations downscaling GFDL-ESM4.1 simulations under SSP-126, SSP-  
148 245, SSP-375, and SSP-585 scenarios (O'Neill et al, 2016). GFDL-ESM4.1 is built on a basis of  
149 GFDL's AM4.0 atmospheric model, which has 49 hybrid vertical layers and approximately  $1^\circ \times$   
150  $1^\circ$  horizontal resolution (Zhao et al., 2018a, 2018b), using the Finite Volume version 3 (FV3;  
151 Lin, 2004) dynamical core with advanced parameterizations of moist convection, clouds,  
152 radiation, topographical drag, and several other physical processes from its previous version. The  
153 land model in GFDL-ESM4.1 is GFDL's Land Model version 4.1 (LM4.1; Shevliakova et al.,  
154 2024), which improved radiative properties for vegetation, soil, and snow, and updated  
155 hydrology in LM4.0. The ocean model component of GFDL-ESM4.1 uses MOM6 (Adcroft et  
156 al., 2019), configured with a nominal resolution of  $\frac{1}{2}$  horizontally and 75 vertical hybrid  $z^*$ -  
157 coordinate layers within the Arbitrary-Lagrangian-Eulerian algorithm (Adcroft & Hallberg,  
158 2006), and the GFDL's Sea Ice Simulator (SIS2; Adcroft et al., 2019). More detailed model  
159 description, additional features, and parameterization settings of GFDL-ESM4.1 can be found in  
160 Dunne et al. (2020). It is noted that the equilibrium climate sensitivity (ECS) of GFDL-ESM4 is

161 approximately 2.6 K, which is at the lower end of the sensitivity range for CMIP6 models  
162 (Dunne et al., 2020; Meehl et al., 2020; Sentman et al., 2026).

163

### 164 2.3 Reanalysis datasets

165 The global reanalysis datasets used to force the retrospective ocean simulation of Ross et al.  
166 (2023) are also used here for bias corrections of ocean lateral boundary conditions, surface  
167 forcings, and river discharge for the historical and future projections derived from GFDL-  
168 ESM4.1 (Table 1). We use the high-resolution ( $1/12^\circ$ ) Global Ocean Physics Reanalysis  
169 (GLORYS12; Lellouche et al., 2021) to derive monthly ocean temperature, zonal and meridional  
170 speeds of ocean current, salinity, and sea surface height (SSH) for 1993-2020 period. We also  
171 use 3-hourly European Centre for Medium-Range Weather Forecast (ECMWF) Reanalysis  
172 version 5 (ERA5) atmospheric reanalysis datasets to derive near-surface zonal and meridional  
173 winds, near-surface air temperature, specific humidity, precipitation, and downwelling short- and  
174 long-wave radiative fluxes (Hersbach et al., 2020).

175 For river discharge, we use the gridded daily Global Flood Awareness System (GloFAS)  
176 version 3.1 reanalysis (Alfieri et al., 2020). Although global river discharge driven by climate  
177 change exhibits a clear positive trend, the projected changes in river discharge in our regional  
178 model domain (i.e., the southern and eastern US seaboards) are insignificant and uncertain  
179 during the first half of the 21st century (Muller et al., 2024). Therefore, we did not consider  
180 future changes in runoff in this single-model downscaling and instead applied the daily mean  
181 climatology (1993–2020) of GloFAS river runoff data for the entire simulation period (1950–  
182 2100). As a result, the potential effects of regional runoff change on nearshore salinity and sea  
183 level are not addressed in this study.

184

185 **Table 1.** Reanalysis products and associated variables used for the bias correction and validation

186 in this study.

| Reanalysis product | Variables                         | Frequency |
|--------------------|-----------------------------------|-----------|
| ERA5               | 2 m temperature                   | 3 hourly  |
|                    | 2 m specific humidity             | 3 hourly  |
|                    | 10 m zonal wind                   | 3 hourly  |
|                    | 10 m meridional wind              | 3 hourly  |
|                    | Sea level pressure                | Daily     |
|                    | Liquid precipitation rate         | Daily     |
|                    | Snowfall rate                     | Daily     |
|                    | Downward shortwave radiative flux | Daily     |
|                    | Downward longwave radiative flux  | Daily     |
| GLORYS12           | Sea water potential temperature   | Monthly   |
|                    | Sea water salinity                | Monthly   |
|                    | Sea water zonal velocity          | Monthly   |

|        |                               |         |
|--------|-------------------------------|---------|
|        | Sea water meridional velocity | Monthly |
|        | Sea surface height            | Monthly |
| GloFAS | River runoff rate             | Daily   |

187

188 2. 4 Mean bias correction

189 To reduce systematic biases in the GFDL-ESM4 outputs, we applied a climatological mean  
190 bias correction to the lateral ocean boundary conditions (BCs) and surface atmospheric forcing  
191 fields using the GLORYS12 and ERA5 reanalysis datasets as follows:

192 
$$\text{Bias-corrected variables} = \text{GFDL-ESM4} + \text{Delta}$$

193 
$$\text{Delta} = \langle \text{Reanalysis} \rangle - \langle \text{GFDL-ESM4} \rangle$$

194 where the GFDL-ESM4 refers to the raw outputs from the GFDL-ESM4 simulations.

195  $\langle \text{Reanalysis} \rangle$  and  $\langle \text{GFDL-ESM4} \rangle$  are the long-term averaged annual cycles from the reanalysis  
196 and GFDL-ESM4 simulations for the 1993-2020 period, respectively. For the GFDL-ESM4  
197 simulations, we merged the data from its historical simulation (1993-2014) with the data from  
198 the future period in each of the four SSP scenarios (2015-2020). The long-term (1993-2020)  
199 means for each month of the year determine the mean annual cycle of the ocean variables, while  
200 the long-term means for each 3-hourly frequency of the year determine the mean annual cycle of  
201 the atmospheric variables. The mean bias correction terms, Delta, were then added to the GFDL-  
202 ESM4 outputs for the entire simulation period (1950-2100) to correct the mean biases. This bias  
203 correction method ensures that mean states of MOM6-NWA12 during the historical period  
204 (1993-2020) are comparable to those in the reanalysis datasets and in Ross et al., (2023).

205 It is noted that our 'Delta method' shares similarities with approaches from previous studies  
206 (Liu et al., 2012; 2015; Alexander et al., 2020; Shin and Alexander, 2020; Pozo-Buil et al.,  
207 2021), which replace model climatology with reanalysis climatology to reduce mean biases.  
208 However, our method fundamentally differs in its treatment of high-frequency atmospheric  
209 forcing. While those previous studies utilized high-frequency atmospheric forcing (i.e., daily  
210 time scales) from historical reanalysis datasets for future projections—thereby assuming that  
211 high-frequency forcing remains unchanged in the future—we retained the model-generated high-  
212 frequency atmospheric variability (e.g., 3-hourly and daily). We took this approach to ensure  
213 more consistent climate projections, recognizing that weather and climate are interdependent.  
214 Indeed, not only does weather depend strongly on low-frequency variability (e.g., weather  
215 conditions during the different phases of ENSO are substantially different), but also weather  
216 statistics can substantially change under future climate conditions (e.g., Cheng et al., 2012;  
217 Jeong and Sushama, 2019).

218 A second notable difference between the methodology herein and past Northwest Atlantic  
219 downscaling studies is the replacement of limited “time slice” experiments with a continuous  
220 integration over the historical and future periods. The continuous integration approach requires  
221 more computational investment (time slices were generally compared across 10-30 year intervals  
222 while continuous integrations required 150 years), but it allows for a more complete analysis of  
223 the emergence of significant differences between scenarios and historical conditions, and  
224 between the scenarios themselves (e.g., Drenkard et al., 2021).

225 Finally, for sea level, we note that both GFDL-ESM4.1 and MOM6-NWA12 utilize the  
226 Boussinesq approximation, which conserves ocean volume. The dynamic sea level in both  
227 models can respond to local density changes driven by local warming and freshening (e.g.,

228 Steinberg et al., 2024). However, these models cannot simulate global mean sea-level (GMSL)  
229 rise caused by thermosteric expansion or added mass from ice melt (e.g., Greatbatch, 1994;  
230 Griffies and Greatbatch, 2012; Griffies et al., 2014). Furthermore, to prevent potential drifts in  
231 the basin-integrated water volume associated with the lateral open boundary conditions, we  
232 explicitly constrain the basin-averaged SSH anomaly to be zero throughout all MOM6-NWA12  
233 simulations. Consequently, the SSH changes derived from MOM6-NWA12 strictly represent the  
234 dynamic redistribution of water mass driven by regional ocean circulation and local steric  
235 adjustments.

236

### 237 **3. Results**

#### 238 3.1. Model validation for the historical period

239 To evaluate the performance of GFDL-ESM4.1 and MOM6-NWA12 in the historical period,  
240 we first compared model-derived climatologies of SST, sea surface salinity (SSS), and surface  
241 current speed against the GLORYS12-derived climatological patterns (Fig. 2 and  
242 Supplementary Fig. S1). The GFDL-ESM4.1 outputs show considerable biases in the SST and  
243 SSS mean patterns. Specifically, the SST has a warm bias  $>3^{\circ}\text{C}$  in the Mid-Atlantic Bight  
244 (MAB), and a cold bias  $>2^{\circ}\text{C}$  in magnitude along the North Atlantic Current path compared to  
245 the data-assimilative GLORYS12 product (Fig. 2d). GFDL-ESM4.1 SSS is saltier than the  
246 GLORYS SSS over the entire domain (Fig. 2e), especially in the MAB and along the US Gulf  
247 Coast, where the bias reaches values  $>3$  PSU. These biases are greatly reduced in the MOM6-  
248 NWA12. For example, the SST biases in the MAB and along the Gulf Stream are  $\sim 1^{\circ}\text{C}$  or lower  
249 (Fig. 2g). The SSS shows a small negative bias, except over the Gulf of Maine, where SSS is  
250 overestimated by about 0.7 PSU (Fig. 2h).

251 The bias patterns for surface ocean velocity reveal that ESM4.1's Loop Current is more  
252 diffusive and extended more northward compared to that in GLORYS12 (Fig. 2f and  
253 Supplementary Fig. S1c). This appears to be due to the coarse horizontal resolution of GFDL-  
254 ESM4.1 ( $\sim 0.5^\circ$ ), which is not fine enough to resolve the Loop Current dynamics (e.g., Liu et al.,  
255 2012; 2015). In addition, ESM4.1's Gulf Stream along the South Atlantic Bight (SAB) is weaker  
256 and slightly shifted away from the US East Coast compared to that in GLORYS12  
257 (Supplementary Fig. S2). In contrast, MOM6-NWA12 shows much improvement of both the  
258 Loop Current and Gulf Stream System (Fig. 2i and Supplementary Fig. S1f). For instance, the  
259 Florida Current (beginning of the Gulf Stream System) in MOM6-NWA12 flows closer to the  
260 coastline compared to that in GFDL-ESM4.1 with speeds exceeding  $1 \text{ m s}^{-1}$ , a pattern similar to  
261 GLORYS12 (Fig. 2f and Fig. 2i).

262 After the separation of the Gulf Stream from the US East Coast, the sluggish flow in GFDL-  
263 ESM4.1 is shifted northward compared to GLORYS12, both at its separation point and as it  
264 travels eastward across the North Atlantic (Fig. 2f ). In contrast, the faster Gulf Stream in  
265 MOM6-NWA12 (Fig. 2i ) is shifted southward at its separation from the coast before  
266 regaining consistency with the data-assimilative GLORYS12 path to the east. This is more  
267 clearly shown in Supplementary Fig. S2, which shows the position of the Gulf Stream core as  
268 a  $15^\circ\text{C}$  isotherm at 200m (e.g., Sanchez-Franks and Zhang, 2015; Hameed et al., 2018; Seidov et  
269 al., 2019; Ross et al., 2023). A northward shift in the Gulf Stream position is typical in low-  
270 resolution ocean models and has been attributed to misrepresentation of nonlinear vorticity  
271 boundary dynamics. While it is not clear why the Gulf Stream in MOM6-NWA12 is shifted  
272 southward, previous studies have indicated that the separation of the Gulf Stream in an eddy-

273 resolving model is very sensitive to the choices made for subgrid scale parameterizations (e.g.,  
274 Chassignet and Marshall, 2008).

275 Consistent with the surface current speed and position of the Gulf Stream, GFDL-ESM4.1  
276 displays a large negative bias in the dynamic sea surface height (SSH), immediately south of the  
277 Gulf Stream core and its extension to the North Atlantic Current. Connected with this, the  
278 recirculation gyre south of the Gulf Stream (35°N- 73°W), known as the Worthington Gyre  
279 (Worthington, 1976), is almost completely absent in GFDL-ESM4.1 (Fig. 3b and d). On the  
280 other hand, the spatial pattern of the dynamic SSH in MOM6-NWA12 exhibits improved  
281 agreement with that in GLORYS12 (Fig. 3c and e), reproducing a Worthington Gyre albeit  
282 weaker than GLORYS12. Given that the Worthington Gyre is a long-term mean rectification of  
283 the Gulf Stream rings and instability waves not resolved at coarse resolution, it is not surprising  
284 that the recirculation gyre is better represented in MOM6-NWA12 while it is nearly absent in  
285 GFDL-ESM4.1.

286 Lastly, we evaluated the volume transports of Northwestern Atlantic boundary current  
287 systems across four zonal transects for the Yucatan Current, Florida Current, Antilles Current,  
288 and the Deep Western Boundary Current (DWBC), which are key components of AMOC  
289 (McCarthy et al., 2015), as shown in Fig. 4. The zonal transection lines for the four current  
290 systems are shown in Fig. 1 (red solid lines). The Antilles Current transport was obtained by  
291 integrating the meridional flow over the upper 500 m across 26.5°N and 77.5°W-75°W.  
292 Similarly, the DWBC transport was obtained by integrating the meridional velocity between  
293 1,000m and 5,000m across 26.5°N and 77.5°W-75°W. GFDL-ESM4.1 simulates a Yucatan  
294 Current transport of  $43.9 \pm 2.87$  Sv, which is about 62% larger than in-situ observation of  $27.5 \pm$   
295  $2.6$  Sv (Athié et al., 2020, Fig. 4a). In contrast, MOM6-NWA12 simulates a transport of 24.2

296  $\pm 1.7$  Sv, which agrees much better with the observed transport. However, the Florida Current  
297 ( $80^{\circ}\text{W}$ - $77.5^{\circ}\text{W}$ ) transport simulated by MOM6-NWA12 ( $24.3 \pm 1.6$  Sv) underestimates the  
298 observation ( $32.5 \pm 3.2$  Sv in Volkov et al., 2024), whereas the Florida Current transport  
299 simulated by GFDL-ESM4 ( $34.4 \pm 2.5$  Sv) is comparable to the observation. This occurs despite  
300 far more realistic surface current speeds in MOM6-NWA12 (i.e., Fig. 2f and i) because the  
301 ESM4.1 Florida Current is far more diffuse and extends to greater depth. Additional sensitivity  
302 simulations indicate that the Florida Current transport in MOM6-NWA12 is quite sensitive to the  
303 eddy viscosity (not shown). By increasing the model diffusivities in MOM6-NWA12, the  
304 simulated Florida Current transport also increased closer to the observed value. However, this  
305 occurred at the expense of other model features, such as the latitude of Gulf Stream separation  
306 from the coast, becoming less realistic. Therefore, the momentum and density diffusivities for  
307 MOM6-NWA12 are unchanged from those used in Ross et al. (2023).

308 As shown in Fig. 4c and d, the simulated transports for both the Antilles Current ( $12.3 \pm$   
309  $4.1$  Sv) and the DWBC ( $-20.8 \pm 8.8$  Sv) in the GFDL-ESM4.1 show substantial disagreement  
310 with observations ( $4.7 \pm 5.2$  Sv for the Antilles Current, Meinen et al., 2019; and  $-31.2 \pm 5.5$  Sv  
311 for the DWBC, Zantopp et al., 2017). MOM6-NWA12, in contrast, better reproduced both the  
312 Antilles Current ( $3.4 \pm 5.6$  Sv) and the DWBC ( $-35.2 \pm 9.5$  Sv). The large biases in GFDL-  
313 ESM4.1 appear to be linked to the overly diffusive and broad Antilles Current and DWBC  
314 (Supplementary Fig. S3).

315 Overall, the high-resolution MOM6-NWA12 configuration generally shows large  
316 improvement in simulating regional ocean circulation and mean conditions compared to the low-  
317 resolution GFDL-ESM4.1. Some deficiencies, however, still exist. Potential impacts of these

318 deficiencies on projected changes, and pathways for future model improvement, will be  
319 discussed in Section 4.

320

## 321 3.2. Future projections

### 322 3.2.1. SST and SSS

323 We first examine the projected spatial changes in SST and SSS derived from the MOM6-  
324 NWA12, comparing the historical period (HIST: 1993–2020) with the late 21st century (L21C:  
325 2073–2100) across four SSP scenarios (SSP-126, SSP-245, SSP-370, and SSP-585). MOM6-  
326 NWA12 shows that SST changes in the future exhibit basin-wide warming with discernable end-  
327 of-century differences (Fig. 5a-e). The domain-averaged SST warming is lowest in the SSP-  
328 126 (0.52 °C) simulation and intensifies progressively in SSP-245 (1.21 °C), SSP-370 (1.86 °C)  
329 and SSP-585 (2.23 °C) simulations. The SST increase is particularly large in the MAB, the Gulf  
330 of Maine, and around the Georges Bank. Temperatures are projected to warm by 4°C in some  
331 areas in the SSP-585 scenario (Fig. 5e). Warming in these regions around the MAB and the  
332 Gulf of Maine (35°N–42°N, 75°W–60°W) is reduced to ~3°C, ~2°C and ~1°C in SSP-370, SSP-  
333 245 and SSP-126, respectively (Fig. 5b-d). Mean warming over the next 30 years (2025-  
334 2055), is expected to ~1-2°C with less separation between scenarios (Supplementary Fig. S4).

335 Similar to the SST change, the amplitude of the SSS change is sensitive to the SSP scenarios  
336 (Fig. 5f-j). The increase in domain-averaged SSS is more pronounced in the higher emission  
337 scenarios (0.13 PSU for SSP-126, 0.22 PSU for SSP-245, 0.41 PSU for SSP-370, and 0.46 PSU  
338 for SSP-585). While SSS tends to increase in the subtropical part of the domain, the largest  
339 projected SSS increase is along the SAB, the continental slope off the MAB and the West

340 Florida Shelf where the future change intensifies progressively under the high-emission  
341 scenarios.

342 The large increases in SST and SSS on the West Florida Shelf and the SAB appear to be  
343 linked to a reduction in shelf-break upwelling due to the projected weakening of the Loop  
344 Current and Gulf Stream (Fig. 6). Additionally, the weakening of the Gulf Stream leads to a  
345 northward shift after its separation from the US East Coast in the late 21st century in all four SSP  
346 scenarios (Fig. 6, Section 3.2.2), consistent with previous studies (e.g., Saba et al., 2016;  
347 Caesar et al., 2018; Bellomo et al., 2021). It appears that the SST increase along the edge of the  
348 MAB is linked to the northward shift of the Gulf Stream and the implied warm water intrusion to  
349 the Slope Sea (Saba et al., 2016). Warming via this mechanism is fortified by commensurate  
350 mean reductions of the advection of cold high-latitude waters from the Labrador Sea.  
351 Interestingly, a narrow region of minimal surface warming is evident immediately south of the  
352 historical Gulf Stream path around 35 °N, 60°W (Fig. 6e). A similar, but smaller area of  
353 minimum surface warming is also evident in the northern GoA, which is largely consistent with  
354 previous studies (Liu et al., 2012, 2015). These regions of minimal SST warming appear to be  
355 linked to the reduced Gulf Stream or the reduced Loop Current, implying a reduction in ocean  
356 heat convergence to these regions (Figs. 6e and 6j).

357 While GFDL-ESM4.1 shows the SSP scenario sensitivity for the amplitude of the future SST  
358 and SSS changes, the pronounced SST warming identified by MOM6-NWA12 in the Mid-  
359 Atlantic Bight (MAB) and Gulf of Maine regions is almost completely absent in GFDL-ESM4.1  
360 ( Fig. 7). This is consistent with the absence of a future northward shift in the Gulf Stream  
361 in the coarse resolution GFDL-ESM4.1 ( Fig. 8) and prior findings of Saba et al., (2015).

362 In summary, MOM6-NWA12 projections of SST, SSS, and surface current speed indicate  
363 that under all four future scenarios, the Northwestern Atlantic basin becomes significantly  
364 warmer, and saltier especially along the US East Coast and the West Florida shelf regions, and  
365 the Gulf Stream becomes considerably weaker and shifts northward. The magnitude of projected  
366 end-of-century changes, however, varies considerably across scenarios. Most notably, the  
367 severity of the impacts projected by the prior worst-case scenario in CMIP5 (i.e., SSP-585) are  
368 progressively mitigated by lower emissions scenarios. Differences between scenarios, however,  
369 are far smaller in the first half of the century.

370

### 371 3.2.2. WBC transports

372 As shown in Figs. 6, the entire WBC system, including the North Brazil Current,  
373 Caribbean Current, Yucatan Current, Loop Current, Florida Current, and the Gulf Stream,  
374 weakens, at least at the surface, consistent with previous future projection studies (e.g., Liu et al.,  
375 2012, 2015; Saba et al, 2016; Alexander et al., 2020; Shin and Alexander, 2020; Beadling et al.,  
376 2018; Roberts et al., 2019). The regions of minimal SST warming appear to be linked to the  
377 reduced Gulf Stream or the reduced Loop Current, implying a reduction in ocean heat  
378 convergence to these regions (Figs. 6e and 6j). To further explore volume transport by the WBCs  
379 system, we examine the temporal changes in the volume transport in the Florida Current,  
380 Yucatan Current, Antilles Current, and the Deep Western Boundary Current (DWBC), as shown  
381 in Fig. 9.

382 The Florida Current exhibits a gradual decline throughout the 21st century across all SSP  
383 scenarios. The largest decrease in the late 21st century is shown in the SSP-585 scenario (Fig.  
384 9a), from  $24.2 \pm 1.7$  Sv in the historical period to  $15.2 \pm 3.5$  Sv in the late 21st century (37.2 %

385 decline) while the smallest decrease in the late 21st century is shown in the SSP-126 scenario  
386 (24.3% decline). The intermediate cases more consistent with current CO<sub>2</sub> trajectories also  
387 exhibit smaller shifts than the prior worst case. The Yucatan Current shows similar rates of  
388 decrease and scenario sensitivity. Under SSP-585, the Yucatan Current transport decreased from  
389  $21.0 \pm 2.1$  Sv in the historical period to  $13.2 \pm 3.1$  Sv in the late 21st century (37.1 % decline,  
390 Fig. 9b) but end-of-century declines are partially mitigated at intermediate and low emissions  
391 cases. The mean transport by the Antilles Current is significantly reduced from  $3.4 \pm 5.6$  Sv in  
392 the historical period to  $-0.72 \pm 4.5$  Sv in the late 21st century, under SSP-585, with relatively  
393 weak variation across scenarios. This suggests that the Antilles Current may disappear (nearly  
394 zero mean transport) after around 2080 (Fig. 9c). This weakening (and the reversal) of the  
395 Antilles Current, which is consistent with a previous modeling study (Cai et al., 2024), may play  
396 a key role in the subtropical gyre recirculation and the upper-ocean stratification in the SAB. Fig.  
397 9d shows that volume transport of the Deep Western Boundary Current (DWBC), which is a  
398 vital return flow component of the AMOC from the high latitudes, exhibits the strongest  
399 response to anthropogenic warming. Particularly under the SSP-585 scenario, the DWBC  
400 transport declines from  $-35.2 \pm 9.5$  Sv in the historical period to  $-20.2 \pm 16.0$  Sv in the late 21st  
401 century (42.7 % decline), reflecting a substantial slowdown in the AMOC under SSP-585 (Fig.  
402 10). This slowdown is once again mitigated in part by intermediate and low emissions scenarios.  
403 As was the case for SST, SSS and current speed, the rate of weakening was not very sensitive  
404 to the emission scenarios before the 2070s. Similarly, the time series of volume transports in the  
405 WBCs system shows a similar rate of decline across all four SSP scenarios until approximately  
406 2070 (Fig. 9). The insensitivity of Northwestern Atlantic WBCs to emission scenarios before  
407 2070s is consistent with the AMOC decline in GFDL-ESM4.1, which is the major contributor to

408 the modulation of the Atlantic WBCs system (Fig. 10). Previous studies (e.g., Weijer et al., 2020;  
409 Baker et al., 2023) found that the rate of AMOC weakening derived from most CMIP6 models  
410 shows limited sensitivity to emission scenarios prior to around 2070, consistent with GFDL-  
411 ESM4.1. It is important to note that the greenhouse gas forcings for the CMIP6 SSP scenarios  
412 begin to diverge after the historical period (~2014), with separation in their radiative forcing  
413 pathways emerging by the mid-21st century. The results that WBC volume transports and  
414 AMOC remain relatively insensitive to these diverging emissions scenarios for several decades  
415 provides critical evidence for a delayed ocean response to greenhouse gas forcing.

416

### 417 3.2.3. Dynamic SSH

418 We next explore dynamic SSH and its projected changes under four SSP scenarios (Fig.  
419 11). Substantial changes in both the amplitude and spatial pattern of dynamic SSH are projected  
420 in the Northwestern Atlantic. In particular, dynamic SSH increases greatly along the West  
421 Florida Shelf (WFS), SAB, MAB, and Georges Bank, and decreases immediately south of the  
422 Gulf Stream (after its separation from the US East Coast) under all four SSP scenarios (Fig. 11).  
423 Given that these changes are largely confined to the region of WBCs and the southern  
424 recirculation (or Worthington) gyre south of the Gulf Stream, the dynamic SSH changes appear  
425 to be directly linked to the substantial weakening of the WBC system (e.g., the Loop Current, the  
426 Florida Current, and the Gulf Stream) and the implied relaxation of the thermocline slope (i.e., a  
427 redistribution of mass) across the WBCs. The projected increases in dynamic SSH along the  
428 WFS, SAB, MAB, and the Georges Bank appear to be largely driven by the AMOC  
429 weakening (e.g., Yin et al., 2009; Little et al., 2017; Weijer et al., 2020). It is noted that the gyre  
430 circulation change potentially contributes to the changes in WBC volume transport. However,  
431 since MOM6-NWA12 is a regional model with open boundaries, we are unable to compute the

432 barotropic streamfunction for the regional domain. Consistent with MOM6-NWA12, GFDL-  
433 ESM4.1 shows an increase in dynamic SSH near the U.S. East Coast and decreases south of the  
434 Gulf Stream (after its separation from the US East Coast) in the late 21st century ( Fig. 12).  
435 An interesting point to note is that MOM6-NWA12 projects a stronger SSH increase in the SAB  
436 than in the MAB while GFDL-ESM4.1 projects a stronger SSH increase north of Cape Hatteras  
437 than in the south. Consistent with this result, Li et al. (2022) show that the projected SSH derived  
438 from a high-resolution Community Earth System Model (CESM) increases more in the SAB  
439 than in the MAB, while that derived from a low-resolution CESM increases more in the MAB  
440 than in the SAB.

441 To further explore the future increases in dynamic SSH along the US South and East Coasts,  
442 we examine the projected dynamic SSH changes over the continental shelf (i.e., depths < 200m)  
443 for five sub-regions, namely the Northern GoA, WFS, SAB, MAB, and Gulf of Maine, as shown  
444 in Fig. 13. The future increase in dynamic SSH is relatively modest in the Northern GoA and  
445 WFS, ranging between 5 and 7 cm during the mid- and late-21st century (2041-2100). These  
446 increases occur mainly during the mid-21st century (2041-2060), after which there is no  
447 significant increase in the dynamic SSH in these shelf regions. Another important feature is that  
448 the dynamic SSH increases in the GoA and WFS (Figs. 13a-b) are not sensitive to the  
449 emission scenarios considered. Given that the dynamic SSH increase in these regions is mainly  
450 driven by the projected weakening of the AMOC and the associated Loop Current, this result  
451 appears to be consistent with the insensitivity in the rate of AMOC's future weakening to the  
452 emission scenarios prior to 2070 ( Fig. 10).

453 In contrast to the Northern GoA and WFS, the projected dynamic SSH changes in the US  
454 East Coast shelf regions (i.e., SAB, MAB, and Gulf of Maine) are significantly larger, ranging

455 between 10 and 20 cm in the late-21st century. Additionally, unlike the US GoA shelf regions  
456 (i.e., Northern GoA and WFS), the increase in dynamic SSH in these regions continues beyond  
457 the mid-21st century to the late-21st century, implying that the weakening of the AMOC and the  
458 associated WBCs have much tighter control over these regions. A systematic tendency toward  
459 greater dynamic SSH changes in higher emissions scenarios also begins to emerge after 2070,  
460 though there is still significant variation around this trend (e.g., SSP-370 has a lower local  
461 dynamic sea level change than SSP245 despite having higher emissions), presumably due to  
462 internal climate variability.

463 Among the five sub-regions considered, the dynamic SSH change in the SAB is subject to  
464 the largest increase. The dynamic SSH in the SAB is projected to increase dramatically after  
465 around 2040, reaching close to 20 cm in the late 21st century compared to that in the historical  
466 period. This suggests that the SAB is the most sensitive to the projected slowdown of the AMOC  
467 and the WBCs in MOM6-NWA12. Specifically, as shown in Fig. 14, a strong negative  
468 correlation exists between the Florida Current transport and the SAB dynamic SSH (e.g., Ezer,  
469 2019; Ezer and Atkinson, 2014) indicating that a -1 Sv reduction in the Florida Current transport  
470 corresponds to about 1.7 cm of dynamic SSH increase in the SAB. This indicates that the SAB is  
471 the future dynamic SSH rise hotspot, potentially posing an increasing flooding risk in the coastal  
472 communities. This appears to be partly due to close proximity of the SAB to the WBC (i.e.,  
473 Florida Current in this case). In the other subregions, the shelf area is too far away from the  
474 WBC (Northern GoA), too wide (WFS), or mediated by the slope water (MAB and Gulf of  
475 Maine).

476 To better understand the relationship between the SAB dynamic SSH increase and the Gulf  
477 Stream weakening, we show the vertical profile of ocean temperature and salinity across 26.5°N

478 during the historical period and their projected changes under the four SSP scenarios (Fig.  
479 15). Fig. 15 clearly illustrates a substantial warming and an increase in salinity, mainly along  
480 the continental slope and shelf. A distinct decrease in density (i.e., lighter water) emerges on the  
481 western side of the Florida Current around 200 m depth (Supplementary Fig. S5). This localized  
482 density reduction reflects a relaxation, or flattening, of the upward-tilted isopycnals along the  
483 Florida coast. Consequently, this flattening of the isopycnals weakens the cross-stream  
484 horizontal density gradient, thereby reducing northward volume transport in the Florida Straits.  
485 Due to reduced bottom Ekman transport and a relaxation, or a flattening, of the upward-tilted  
486 isopycnals associated with a weakened Gulf Stream, upwelling decreases along the continental  
487 slope and shelf, limiting the supply of cold and relatively fresh subsurface water from underneath  
488 the Gulf Stream. This indicates that the warm and salty Gulf Stream water penetrates deeper into  
489 the continental slope and shelf region due to the weakening of the Gulf Stream. This mass  
490 redistribution from the open ocean to the coastal region is also directly responsible for the large  
491 projected increase in dynamic SSH across the SAB, which is consistent with the historical  
492 analysis of Steinberg et al. (2024). These future changes in ocean conditions near the coastline  
493 are also projected in West Florida. The reduction of the Loop Current leads to an increase in  
494 dynamic SSH across West Florida and a significant reduction in the upwelling of cold and  
495 relatively fresh subsurface water. This, in turn, results in warm, salty Loop Current water  
496 penetrating deeper into the WFS (Fig. 16).

497 In the MAB (30°N–41°N, 76°W–67°W), the weakening and shoreward shift of the Gulf  
498 Stream in the late 21st century drives an increase in ocean temperature and salinity along the  
499 continental slope and shelf (Fig. 17). The maximum SSH anomaly is observed near the core  
500 location of the shifted Gulf Stream. Specifically, projected SSH increases on the coastal side of

501 the current while decreasing on the open-ocean side. This differential change results in a reduced  
502 cross-stream SSH gradient (slope), consistent with the geostrophic weakening of the flow.

503 Finally, we emphasize that the dynamical SSH changes described in this study would occur  
504 in addition to the GMSL rise associated with ocean warming and glacial and ice-sheet melt. As  
505 described in the methods, MOM6-NWA12 can respond to local density changes driven by local  
506 warming and freshening (e.g., Steinberg et al., 2024), GMSL rise is not directly reflected in the  
507 model simulation due to the Boussinesq approximation. Therefore, to explore the total coastal  
508 SSH change (i.e., dynamic SSH changes plus GMSL rise) in the late 21st century, the dynamic  
509 SSH changes derived from MOM6-NWA12 are combined with the GMSL change. According to  
510 the IPCC AR6 report (IPCC, 2021), the projected GMSL rise by the late 21st century relative to  
511 the historical period is 0.38 m for SSP-126, 0.47 m for SSP-245, 0.56 m for SSP-370, and 0.64 m  
512 for SSP-585, respectively. Specifically, in the SAB under the SSP-585 scenario, the dynamic sea  
513 level increase by the late 21st century (~0.2 m) accounts for nearly 25% of the total sea level  
514 increase. This highlights that the SAB could experience extreme and compounding (e.g., high  
515 tides and storm surges) coastal flooding risks in the future.

#### 516 **4. Summary and Discussion**

517 This study describes and evaluates the dynamically downscaled physics-only MOM6-  
518 NWA12 simulations of GFDL-ESM4, and then explores future changes of the Northwest  
519 Atlantic Ocean under four CMIP6 emission scenarios (SSP-126, SSP-245, SSP-370, and SSP-  
520 585). Validation of model outputs against direct ocean observational and reanalysis data shows  
521 that the biases in GFDL-ESM4 are significantly reduced in MOM6-NWA12, particularly in the  
522 spatial SST and SSS patterns, as well as the Gulf Stream's path and volume transport. For  
523 instance, while GFDL-ESM4 exhibits pronounced warm and high salinity biases along the US

524 East Coast and a northward shift of the Gulf Stream, MOM6-NWA12 simulates improved  
525 representation of these key features, including a better alignment of the Gulf Stream path with  
526 observations. Furthermore, MOM6-NWA12 captures the spatial pattern of SSH much more  
527 accurately, as well as the WBCs (i.e., Florida Current, Yucatan Current, Antilles Current, and  
528 DWBC).

529 The projections derived from MOM6-NWA12 show significant changes in SST, SSS and the  
530 WBCs under the four SSP scenarios considered. The magnitude of end-of-century changes is  
531 strongly scenario-dependent: pronounced SST warming in the MAB and Gulf of Maine,  
532 exceeding 4°C in some areas, emerges as a distinct feature of the prior “worst-case” high-  
533 emission scenarios (SSP-585), partial mitigation is apparent in intermediate trajectories more  
534 consistent with current CO2 trajectories (SSP-370, SSP-245), and this signal remains modest  
535 under low-emission scenarios (SSP-126). The amplified warming and salinification along the US  
536 South and East Coasts appears to be linked to a weakening of the Loop Current and Gulf Stream  
537 (e.g., Liu et al., 2012, 2015; Saba et al., 2016) alongside a shoreward and northward shift of the  
538 Gulf Stream following its separation from the coast (e.g., Yin et al., 2009; Saba et al., 2016;  
539 Bellomo et al., 2021; Li et al., 2022). In addition, as discussed in New et al. (2021), the MAB  
540 and the Gulf of Maine are also strongly influenced by the Labrador Current and the Labrador  
541 Slope Water (LSLW). The Slope Current in MOM6-NWA12 shows a large bias in its position  
542 and the strength. More specifically, it is much weaker compared to that in GLORYS12, and is  
543 replaced by northward flow in the upper 400m or so (Supplementary Fig. 6). Another core of  
544 southward flow appears immediately shoreward of the Gulf Stream in MOM6-NWA12. Since it  
545 is positioned away from the continental slope (near 73°W), it is referred to as the northern  
546 recirculation flow of the Gulf Stream. In the future scenarios, both the northern recirculation

547 flow and the Slope Current (below 600m) drastically weaken. The Gulf Stream also weakens and  
548 its core shifts shoreward. In the SSP370 and SSP585 scenarios, the Gulf Stream core is  
549 positioned along the continental slope. Thus, both the northern recirculation flow and the Slope  
550 Current (below 600m or so) completely disappear in those high emission scenarios. Therefore,  
551 despite a large bias in the location and strength of the Slope Current in MOM6-NWS12, we can  
552 still conclude that the future warming and saltening in the MAB, shown in Fig. 17, are the result  
553 of a compounding effect - a weakening and shoreward shift of the Gulf Stream combined with  
554 reduced advection of cold, fresh Labrador Sea waters.

555 A consistent feature across all projections is the significant deceleration of the surface speed  
556 and volume transport of the four WBCs (i.e., Yucatan Current, Florida Current, Antilles Current  
557 and DWBC), which aligns well with the significant weakening of the AMOC. Reductions in the  
558 meridional transports of the four WBCs remain insensitive to emission scenarios until the 2070s,  
559 after which they diverge significantly (ranging from ~23% in SSP-126 to ~38% in SSP-585  
560 scenarios).

561 The projections also suggest that the slowdown of the WBCs leads to an increase in dynamic  
562 SSH along the US South and East Coasts, which is largest in the SAB. The increased dynamic  
563 SSH in these regions is directly related to the weakening of the WBCs and the associated  
564 redistribution of the mass across the WBCs (Minobe et al., 2017). As such, a strong negative  
565 correlation exists between the Florida Current transport and the dynamic SSH in the SAB, for  
566 example. Further analysis shown in Fig. 15 indicates that the weakening of the Florida Current  
567 accompanies a substantial reduction of upwelling of cold and fresh subsurface water to the  
568 continental slope and shelf region. The associated decrease in nutrient supply, implied by the  
569 reduced upwelling, has important implications for the marine ecosystems and productivity in the

570 SAB, as the Gulf Stream-induced upwelling represents the main source of nutrients to the SAB  
571 outer and mid shelf (e.g., Lee et al., 1991; Gomez et al., 2026).

572 While this study has mostly focused on describing the future mean changes across scenarios,  
573 there are several areas that require further investigation, such as the changes in the seasonal  
574 circulation patterns and their impact on the anomalous ocean conditions. This could be relevant,  
575 for example, in the MAB where seasonal changes in wind stress drives the annual sea level  
576 height variability (e.g., Yang and Chen, 2025). It could also be relevant for the SAB where the  
577 seasonal wind stress changes impact coastal temperature and cross-shore interchanges through  
578 upwelling (e.g., Castelao et al., 2011; Yuan et al., 2017). Therefore, further study is needed to  
579 explore future changes in the seasonality of WBCs, and their impacts.

580 Lastly, building on these results derived from physics-only simulations, we plan to couple the  
581 physical ocean model with the Carbon, Ocean Biogeochemistry and Lower Trophics (COBALT,  
582 Stock et al., 2020, 2025) model to explore future changes in ocean ecosystems in the Northwest  
583 Atlantic. Additionally, we will expand the scenario-focused ensemble presented here to include  
584 multiple GCMs to fully assess the potential range of the future changes in the Northwest  
585 Atlantic.

586

## 587 **Acknowledgements**

588 We would like to sincerely thank two anonymous reviewers for their thorough reviews and  
589 thoughtful comments and suggestions, which led to a significant improvement of the paper. We  
590 also thank Liz Drenkard for helpful comments and suggestions. This study was supported by the  
591 NOAA's Changing Ecosystems, and Fisheries Initiative (CEFI) and the NOAA award Number  
592 NA24OARX405C0044-T1-01. This study was also carried out under the auspices of the

593 Cooperative Institute for Marine and Atmospheric Studies (CIMAS) (NOAA cooperative  
594 agreement NA20OAR4320472), the Northern Gulf Institute (NGI) (NOAA cooperative  
595 agreement NA21OAR4320190), and supported by NOAA’s Oceanic and Atmospheric Research  
596 and NOAA’s Atlantic Oceanographic and Meteorological Laboratory.

597

### 598 **Code availability**

599 The source code for each component of the MOM6-NWA12 model has been archived by  
600 Ross et al. (2023) and the GitHub repositories are located at [https://github.com/NOAA-](https://github.com/NOAA-GFDL/CEFI-regional-MOM6)  
601 [GFDL/CEFI-regional-MOM6](https://github.com/NOAA-GFDL/CEFI-regional-MOM6). All codes for analyses were performed using the Grid Analysis  
602 and Display System (GrADS), which is publicly available from the Center for Ocean-Land-  
603 Atmosphere Studies at <http://cola.gmu.edu/grads> and NCL, which is publicly available from the  
604 NCAR Command Language (NCL) at <https://www.ncl.ucar.edu/>. The GrADS, NCL, and Fortran  
605 codes used to perform the analyses can be accessed upon request to D. K.

606

### 607 **Data availability**

608 The model outputs derived from the MOM6-NWA12 future projections under four SSP  
609 scenarios will be available at CEFI portal soon ([https://psl.noaa.gov/cefi\\_portal/](https://psl.noaa.gov/cefi_portal/)). GLORYS12  
610 reanalysis dataset is available at <https://data.marine.copernicus.eu/product/>. ERA5 reanalysis  
611 dataset is available at <https://cds.climate.copernicus.eu/datasets/reanalysis-era5-single-levels>.  
612 GFDL-ESM4 outputs are freely available at the CMIP6 archive  
613 (<https://aims2.llnl.gov/search/cmip6/>).

614

### 615 **Author Contribution**

616 D Kim, AC Ross, SI Shin and SK Lee contributed source code for the downscaling system for  
617 the regional MOM6. D Kim, SI Shin and SK Lee contributed to preparation of model input files.  
618 D Kim, FA Gomez and SK Lee contributed to evaluation and interpretation of the model results.  
619 D Kim and SK Lee prepared the initial draft of the manuscript. All coauthors participated in  
620 discussions during various stages of the model development and evaluation and read and  
621 approved the final version of the manuscript.

622

### 623 **Competing interests**

624 Dr. Charles A. Stock (one of co-authors) serves as editor for the special issue to which this paper  
625 belongs.

626

### 627 **References**

- 628 1. Adcroft, A., Anderson, W., Balaji, V., Blanton, C., Bushuk, M., Dufour, C. O., Dunne, J. P.,  
629 Griffies, S. M., Hallberg, R., Harrison, M. J., Held, I. M., Jansen, M. F., John, J. G., Krasting,  
630 J. P., Langenhorst, A. R., Legg, S., Liang, Z., McHugh, C., Radhakrishnan, A., Reichl, B. G.,  
631 Rosati, T., Samuels, B. L., Shao, A., Stouffer, R., Winton, M., Wittenberg, A. T., Xiang, B.,  
632 Zadeh, N., and Zhang, R.: The GFDL Global Ocean and Sea Ice Model OM4.0: Model  
633 Description and Simulation Features, *Journal of Advances in Modeling Earth Systems*, 11,  
634 3167–3211, <https://doi.org/10.1029/2019MS001726>, 2019.
- 635 2. Adcroft, A., and Campin, J.-M.: Rescaled height coordinates for accurate representation of  
636 free-surface flows in ocean circulation models, *Ocean Modelling*, 7, 269–284,  
637 <https://doi.org/10.1016/j.ocemod.2003.09.003>, 2004.

- 638 3. Adcroft, A., and Hallberg, R.: On methods for solving the oceanic equations of motion in  
639 generalized vertical coordinates, *Ocean Modelling*, 11, 224–233,  
640 <https://doi.org/10.1016/j.ocemod.2004.12.007>, 2006
- 641 4. Alexander, M. A., and Scott, J. D.: The Role of Ekman Ocean Heat Transport in the Northern  
642 Hemisphere Response to ENSO, *Journal of Climate*, 21, 5688–5707,  
643 <https://doi.org/10.1175/2008JCLI2382.1>, 2008.
- 644 5. Alexander, M. A., Shin, S., Scott, J. D., Curchitser, E., and Stock, C.: The Response of the  
645 Northwest Atlantic Ocean to Climate Change, *Journal of Climate*, 33, 405–428,  
646 <https://doi.org/10.1175/JCLI-D-19-0117.1>, 2020.
- 647 6. Alfieri, L., Lorini, V., Hirpa, F. A., Harrigan, S., Zsoter, E., Prudhomme, C., and Salamon,  
648 P.: A Global Streamflow Reanalysis for 1980–2018, *Journal of Hydrology*, 6, 100049,  
649 <https://doi.org/10.1016/j.hydroa.2019.100049>, 2020.
- 650 7. Athié, G., Sheinbaum, J., Leben, R., Ochoa, J., Shannon, M. R., and Candela, J.: Interannual  
651 variability in the Yucatan Channel flow, *Geophysical Research Letters*, 42, 1496–1503,  
652 [doi:10.1002/2014GL062674](https://doi.org/10.1002/2014GL062674), 2015.
- 653 8. Baker, J. A., Bell, M. J., Jackson, L. C., Renshaw, R., Vallis, G. K., Watson, A.J., and Wood,  
654 R. A.: Overturning pathways control AMOC weakening in CMIP6 models. *Geophysical  
655 Research Letters*, 50, e2023GL103381. <https://doi.org/10.1029/2023GL103381>, 2023.
- 656 9. Bell, R. J., Richardson, D. E., Hare, J. A., Lynch, P. D., and Fratantoni, P. S.: Disentangling  
657 the effects of climate, abundance, and size on the distribution of marine fish: an example  
658 based on four stocks from the Northeast US shelf, *ICES Journal of Marine Science*, 72,  
659 1311–1322, <https://doi.org/10.1093/icesjms/fsu217>, 2015.

- 660 10. Beadling, R. L., Russell, J. L., Stouffer, R. J. & Goodman, P. J.: Evaluation of subtropical  
661 North Atlantic Ocean circulation in CMIP5 models against the observational array at 26.5°N  
662 and its changes under continued warming. *Journal of Climate*. 31, 9697-9718,  
663 <https://doi.org/10.1175/jcli-d-17-0845.1>, 2018.
- 664 11. Bellomo, K., Angeloni, M., Corti, S. and Hardenberg, J.: Future climate change shaped by  
665 inter-model differences in Atlantic meridional overturning circulation response, *Nature*  
666 *Communications*, 12, 3659, <https://doi.org/10.1038/s41467-021-24015-w>, 2021.
- 667 12. Caesar, L., Rahmstorf, S., Robinson, Feulner, G., and Saba, V.: Observed fingerprint of a  
668 weakening Atlantic Ocean overturning circulation, *Nature*, 556, 191–196,  
669 <https://doi.org/10.1038/s41586-018-0006-5>, 2018.
- 670 13. Cai, J., Yang, H., Chen, Z., and Wu. L.: The disappearing Antilles Current dominates the  
671 weakening meridional heat transport in the North Atlantic Ocean under global warming,  
672 *Environmental Research Letters*, 19, 044049, <https://doi.org/10.1088/1748-9326/ad3567>,  
673 2024.
- 674 14. Castelao, R.: Intrusions of Gulf Stream waters onto the South Atlantic Bight shelf, *Journal of*  
675 *Geophysical Research: Oceans*, 116, C10011, <https://doi.org/10.1029/2011JC007178>, 2011.
- 676 15. Chassignet, E., and Marshall. D.: Gulf Stream separation in numerical ocean models, In  
677 *Ocean Modeling in an Eddy Regime*, *Geophysical Monograph Series*, 177, 2008.
- 678 16. Cheng, C. S., Li, G., Li, Q., Auld, H., and Fu, C.: Possible Impacts of Climate Change on  
679 Wind Gusts under Downscaled Future Climate Conditions over Ontario, Canada, *Journal of*  
680 *Climate*, 25, 3390–3408, <https://doi.org/10.1175/JCLI-D-11-00198.1>, 2012.
- 681 17. Dong, S., Baringer, M., and Goni, G.: Slowdown of the Gulf Stream during 1993–2016.  
682 *Scientific Reports*, 9, 6672, <https://doi.org/10.1038/s41598-019-42820-8>, 2019.

- 683 18. Domingues, R., Goni, G., Baringer, M., and Volkov, D.: What caused the accelerated sea  
684 level changes along the U.S. East Coast during 2010-2015?, *Geophysical Research Letters*,  
685 45, 13367–13376, <https://doi.org/10.1029/2018GL081183>, 2018.
- 686 19. Drenkard, E. J., Stock, C., Ross, A. C., Dixon, K. W., Adcroft, A., Alexander, M., Balaji, V.,  
687 Bograd, S. J., Butenschön, M., Cheng, W., Curchitser, E., Lorenzo, E. D., Dussin, R.,  
688 Haynie, A. C., Harrison, M., Hermann, A., Hollowed, A., Holsman, K., Holt, J., Jacox, M.  
689 G., Jang, C. J., Kearney, K. A., Muhling, B. A., Buil, M. P., Saba, V., Sandø, A. B.,  
690 Tommasi, D., and Wang, M.: Next-generation regional ocean projections for living marine  
691 resource management in a changing climate, *ICES Journal of Marine Science*, 78, 1969–  
692 1987, <https://doi.org/10.1093/icesjms/fsab100>, 2021.
- 693 20. Dunne, J. P., Horowitz, L. W., Adcroft, A. J., Ginoux, P., Held, I. M., John, J. G., Krasting, J.  
694 P., Malyshev, S., Naik, V., Paulot, F., Shevliakova, E., Stock, C. A., Zadeh, N., Balaji, V.,  
695 Blanton, C., Dunne, K. A., Dupuis, C., Durachta, J., Dussin, R., Gauthier, P. P. G., Griffies,  
696 S. M., Guo, H., Hallberg, R. W., Harrison, M., He, J., Hurlin, W., McHugh, C., Menzel, R.,  
697 Milly, P. C. D., Nikonov, S., Paynter, D. J., Ploshay, J., Radhakrishnan, A., Rand, K., Reichl,  
698 B. G., Robinson, T., Schwarzkopf, D. M., Sentman, L. T., Underwood, S., Vahlenkamp,  
699 H., and Winton, M.: The GFDL Earth System Model Version 4.1 (GFDL-ESM 4.1): Overall  
700 coupled model description and simulation characteristic, *Journal of Advances in Modeling  
701 Earth Systems*, 12, e2019MS002015. <https://doi.org/10.1029/2019MS002015>, 2020.
- 702 21. Ezer, T.: Detecting changes in the transport of the Gulf Stream and the Atlantic overturning  
703 circulation from coastal sea level data: The extreme decline in 2009–2010 and estimated  
704 variations for 1935–2012, *Global and Planetary Change*, 129, 23–36.  
705 <https://doi.org/10.1016/j.gloplacha.2015.03.002>, 2015.

- 706 22. Ezer, T.: Regional differences in sea level rise between the Mid-Atlantic Bight and the South  
707 Atlantic Bight: Is the Gulf Stream to blame?, *Earth's Future*, 7, 771–783.  
708 <https://doi.org/10.1029/2019EF001174>, 2019.
- 709 23. Ezer, T., and Atkinson, L. P.: Accelerated flooding along the U.S. EastCoast: On the impact  
710 of sea-level rise,tides, storms, the Gulf Stream, and the North Atlantic Oscillations, *Earth's*  
711 *Future*, 2, 362–382,doi:10.1002/2014EF000252, 2014.
- 712 24. Ezer, T., Atkinson, L. P., Corlett, W. B., and Blanco, J. L.: Gulf Stream's induced sea level  
713 rise and variability along the US mid-Atlantic coast, *Journal of Geophysical Research:*  
714 *Oceans*, 118, 685–697, <https://doi.org/10.1002/jgrc.20091>, 2013.
- 715 25. Friedrichs, M. A. M., St-Laurent, P., Xiao, Y., Hofmann, E., Hyde, K., Mannino, A., Najjar,  
716 R. G., Narváez, D. A., Signorini, S.R., Tian, H., Wilkin, J., Yao, Y., Xue, J.: Ocean  
717 circulation causes strong variability in the Mid-Atlantic Bight nitrogen budget. *Journal of*  
718 *Geophysical Research: Oceans*, 124, 113–134. <https://doi.org/10.1029/2018JC014424>, 2019.
- 719 26.
- 720 27. Goddard, P. B., Yin, J., Griffies, S. M., and Zhang, S.: An extreme event of sea-level rise  
721 along the Northeast coast of North America in 2009–2010, *Nature Communications*, 6,  
722 <https://doi.org/10.1038/ncomms7346>, 2015.
- 723 28. Gomez, F.A., Lee, S.K., Hernandez, F.J., Chiaverano, L.M., Muller-Karger, F.E., Liu, Y.,  
724 and Lamkin, J.T.: ENSO-induced co-variability of Salinity, Plankton Biomass and Coastal  
725 Currents in the Northern Gulf of Mexico. *Scientific reports*, 9, 178,  
726 <https://doi.org/10.1038/s41598-018-36655-y>, 2019.
- 727 29. Gomez, F. A., Lee, S.-K., Stock, C. A., Ross, A.C., Resplandy, L., Siedlecki, S.A., Tagklis,  
728 F., and Salisbury, J. E.: RC4USCoast: A river chemistry dataset for regional ocean model

729 applications in the U.S. East, Gulf of Mexico, and West Coasts, *Earth System Science Data*,  
730 <https://doi.org/10.5194/essd-2022-341>, 2022.

731 30. Gomez, F. A., Ross, A. C., Lee, S.-K., Volkov, D., Kim, D., John, J. G., & Stock, C. A.:  
732 Wind control of the interannual ocean-biogeochemical variability in the South Atlantic Bight,  
733 *Journal of Geophysical Research: Oceans*, 131, e2025JC023322, 2026.

734 31. Gomez, F.A., Wanninkhof, R., Barbero, L., and Lee, S.-K.: Mississippi River Chemistry  
735 Impacts on the Interannual Variability of Aragonite Saturation State in the Northern Gulf of  
736 Mexico, *Journal of Geophysical Research: Oceans*, 129 , e2023JC020436, 2024.

737 32. Gomez, F.A., Wanninkhof, R., Barbero, L., Lee, S.K., and Hernandez, F. J.: Seasonal  
738 patterns of surface inorganic carbon system variables in the Gulf of Mexico inferred from a  
739 regional high-resolution ocean biogeochemical model, *Biogeosciences*, 17, 1685–1700.  
740 <https://doi.org/10.5194/bg-17-1685-2020>, 2020.

741 33. Greatbatch, R. J.: A note on the representation of steric sea level in models that conserve  
742 volume rather than mass. *Journal of Geophysical Research: Oceans*, 12, 767–12,771, 1994.

743 34. Griffies, S. M., and Greatbatch, R. J.: Physical processes that impact the evolution of global  
744 mean sea level in ocean climate models, *Ocean Modelling*, 51, 37–72, 2012.

745 35. Griffies, S. M., Yin, J., Durack, P. J., Goddard, P., Bates, S. C., Behrens, E., Bentsen, M., Bi,  
746 D., Biastoch, A., Böning, C., Bozec, A., Chassignet, E., Danabasoglu, G., Danilov, S.,  
747 Domingues, C. M., Drange, H., Farneti, R., Fernandez, E., Greatebatch, R. J., Holland, D.  
748 M., Ilicak, M., Large, W. G., Lorbacher, K., Lu, J., Marsland, S. J., Mishra, A., Nurser, A. J.  
749 G., Salas y Mélia, D., Palter, J. B., Samuels, B. L., Schröter, Schwarzkopf, F. U., Sidorenko,  
750 D., Treguier, A.-M., Tseng, Y. H., Tsujino, H., Uotila, P., Valcke, S., Voltaire, A., Wang,  
751 Q., Winton, M., and Zhang, X.: An assessment of global and regional sea level for years

- 1993–2007 in a suite of interannual CORE-II simulations, *Ocean Modelling*, 78, 35-89,  
<https://doi.org/10.1016/j.ocemod.2014.03.004>, 2014.
36. Hameed, S., C. Wolfe, L. P., and Chi, L.: Impact of the Atlantic Meridional Mode on Gulf Stream North Wall Position, *Journal of Climate*, 31, 8875–8894,  
<https://doi.org/10.1175/JCLI-D-18-0098.1>, 2018.
37. Hermans, T. H. J., Gregory, J. M., Palmer, M. D., Ringer, M. A., Katsman, C. A., and Slangen, A. B. A.: Projecting global mean sea-level change using CMIP6 models, *Geophysical Research Letters*, 48, e2020GL092064. <https://doi.org/10.1029/2020GL092064>, 2021.
38. Hersbach, H., Bell, B., Berrisford, P., Hirahara, S., Horányi, A., Muñoz-Sabater, J., Nicolas, J., Peubey, C., Radu, R., Schepers, D., Simmons, A., Soci, C., Abdalla, S., Abellan, X., Balsamo, G., Bechtold, P., Biavati, G., Bidlot, J., Bonavita, M., De Chiara, G., Dahlgren, P., Dee, D., Diamantakis, M., Dragani, R., Flemming, J., Forbes, R., Fuentes, M., Geer, A., Haimberger, L., Healy, S., Hogan, R. J., Hólm, E., Janisková, M., Keeley, S., Laloyaux, P., Lopez, P., Lupu, C., Radnoti, G., de Rosnay, P., Rozum, I., Vamborg, F., Villaume, S., and Thépaut, J.-N.: The ERA5 Global Reanalysis, *Quarterly Journal of the Royal Meteorological Society*, 146, 1999–2049, <https://doi.org/10.1002/qj.3803>, 2020.
39. Huang, L., Volkov, D. L., Dong, S., and Schmid, C.: On the rapid warming in the subtropical North Atlantic in 2011–2021, *Geophysical Research Letters*, 52, e2025GL116280. <https://doi.org/10.1029/2025GL116280>, 2025.
40. Intergovernmental Panel On Climate Change (Ipc). *Climate Change 2021 – The Physical Science Basis: Working Group I Contribution to the Sixth Assessment Report of the*

774 Intergovernmental Panel on Climate Change. (Cambridge University Press, 2023).  
775 doi:10.1017/9781009157896.

776 41.

777 42. Jeong, D.I., and Sushama, L.: Projected Changes to Mean and Extreme Surface Wind Speeds  
778 for North America Based on Regional Climate Model Simulations, *Atmosphere*, 10, 497,  
779 <https://doi.org/10.3390/atmos10090497>, 2019.

780 43. Jin, C., Liu, H., Lin, P., Lyu, K., and Li, Y.: Uncertainties in the projection of stereodynamic  
781 sea level in CMIP6 models, *Geophysical Research Letters*, 52, e2024GL113691.  
782 <https://doi.org/10.1029/2024GL113691>, 2025.

783 44. Karnauskas, M., Schirripa, M.J., Craig, K., Cook, G, Kelble, C., Agar, J., Black, B., Enfield,  
784 D., Lindo-Atichati, D., Muhling, B., Purcell, K., Richards, P., and Wang C. Evidence of  
785 climate-driven ecosystem reorganization in the Gulf of Mexico, *Global Change Biology*, 21,  
786 2554–2568, 2015.

787 45. Karnauskas, M., Schirripa, M.J., Kelble, C.K., Cook, G.S., and Craig, J.K.: Ecosystem status  
788 report for the Gulf of Mexico, NOAA Technical Memorandum NMFS-SEFSC-653, 2013

789 46. Koul, V., Ross, A. C., Stock, C., Zhang, L., Delworth, T., and Wittenberg, A.: A predicted  
790 pause in the rapid warming of the Northwest Atlantic Shelf in the coming decade,  
791 *Geophysical Research Letters*, 51, e2024GL110946, <https://doi.org/10.1029/2024GL110946>,  
792 2024.

793 47. Lee, T. N., Yoder, J. A., and Atkinson, L. P.: Gulf Stream frontal eddy influence on  
794 productivity of the 857 southeast US Continental Shelf, *Journal of Geophysical Research:*  
795 *Oceans*, 96, 191–205, <https://doi.org/10.1029/91jc02450>, 1991.

- 796 48. Lellouche, J., Greiner, E., Bourdallé-Badie, R., Garric, G., Melet, A., Dréville, M., Bricaud,  
797 C., Hamon, M., Le Galloudec, O., Regnier, C., Candela, T., Testut, C., Gasparin, F.,  
798 Ruggiero, G., Benkiran, M., Drillet, Y., and Le Traon, P.: The Copernicus Global 1/12  
799 Oceanic and Sea Ice GLORYS12 Reanalysis, *Frontiers in Earth Science*, 9, 698876,  
800 <https://doi.org/10.3389/feart.2021.698876>, 2021.
- 801 49. Levermann, A., Griesel, A., Hofmann, M., Montoya, M., and Rahmstorf, S.: Dynamic sea  
802 level changes following changes in the thermohaline circulation, *Climate Dynamics*, 24,  
803 347–354, <https://doi.org/10.1007/s00382-004-0505-y>, 2005.
- 804 50. Li, D., Chang, P., Yeager, S. G., Danabasoglu, G., Castruccio, F. S., Small, Wang, H.,  
805 Zhang, Q., and Gopal, A.: The impact of horizontal resolution on projected sea-level rise  
806 along US east continental shelf with the community earth system model, *Journal of Advances  
807 in Modeling Earth Systems*, 14, e2021MS002868, 2022.
- 808 51. Lin, S. J.: A “vertically Lagrangian” finite-volume dynamical core for global models,  
809 *Monthly Weather Review*, 132, 2293–2307. 2004.
- 810 52. Little, C. M., Hu, A., Hughes, C. W., McCarthy, G. D., Piecuch, C. G., Ponte, R. M., and  
811 Thomas, M. D.: The Relationship between U.S. East Coast sea level and the Atlantic  
812 Meridional Overturning Circulation: A review, *Journal of Geophysical Research: Oceans*, 124,  
813 6435–6458, <https://doi.org/10.1029/2019JC015152>, 2019.
- 814 53. Little, C. M., Piecuch, C. G., and Ponte, R. M.: On the relationship between the meridional  
815 overturning circulation, alongshore wind stress, and United States East Coast sea level in the  
816 Community Earth System Model Large Ensemble, *Journal of Geophysical Research: Oceans*  
817 122, 4554–4568, <https://doi.org/10.1002/2017JC012713>, 2017.

- 818 54. Liu, Y., Lee, S.-K., Enfield, D. B., Muhling, B. A., Lamkin, J. T., Muller-Karger, F. E., and  
819 Roffer, M. A.: Potential impact of climate change on the Intra-Americas Sea: Part-1. A  
820 dynamic downscaling of the CMIP5 model projections, *Journal of Marine Systems*, 148, 56-  
821 69, <https://doi.org/10.1016/j.jmarsys.2015.01.007>, 2015.
- 822 55. Liu, Y., Lee, S.-K., Muhling, B.A., Lamkin, J.T., and Enfield, D.B.: Significant reduction of  
823 the Loop Current in the 21st century and its impact on the Gulf of Mexico, *Journal of*  
824 *Geophysical Research:Oceans*, 117, C05039. <http://dx.doi.org/10.1029/2011JC007555>, 2012.
- 825 56. McCarthy, G. D., Smeed D.A., Johns W.E., Frajka-Williams E., Moat B.I., Rayner D.,  
826 Baringer M.O., Meinen C.S., Collins, J., and Bryden H.L.: Measuring the Atlantic  
827 Meridional Overturning Circulation at 26°N. *Progress in Oceanography*, 130, 91-111,  
828 <http://dx.doi.org/10.1016/j.pocean.2014.10.006>, 2015.
- 829 57. Meehl, G. A., Senior, C. A., Eyring, V., Flato, G., Lamarque, J.-F., Stouffer, R. J., Taylor, K.  
830 E., and Schlund, M.: Context for interpreting equilibrium climate sensitivity and transient  
831 climate response from the CMIP6 Earth system models. *Science Advances*, 6, eaba1981,  
832 2020.
- 833 58. Meinen, C. S., Johns, W. E., Moat, B. I., Smith, R. H., Johns, E. M., Rayner, D., Frajka-  
834 Williams, E., Garcia, R.F., and Garzoli, S. L.: Structure and variability of the Antilles  
835 Current at 26.5°N, *Journal of Geophysical Research: Oceans*, 124, 3700–3723.  
836 <https://doi.org/10.1029/2018JC014836>, 2019.
- 837 59. Minobe, S., Terada, M., Qiu, B., and Schneider, N.: Western boundary sea level: A theory,  
838 rule of thumb, and application to climate models, *Journal of Physical Oceanography*, 47,  
839 957–977, <https://doi.org/10.1175/JPO-D-16-0144.1>, 2017.

- 840 60. Muller-Karger, F. E., Smith, J. P., Werner, S., Chen, R., Roffer, M., Liu, Y., Muhling, B.,  
841 Lindo-Atichati, D., Lamkin, J., Cerdeira-Estrada, S., and Enfield, D. B.: Natural variability of  
842 surface oceanographic conditions in the offshore Gulf of Mexico, *Progress in Oceanography*,  
843 134, 54–76. 2015.
- 844 61. New, A. L., Smeed, D. A., Czaja A., Blaker A.T., Mecking J. V., Mathews J.P., and  
845 Sanchez-Franks A.: Labrador Slope Water connects the subarctic with the Gulf Stream.  
846 *Environ. Res. Lett.* 16, 084019, <https://doi.org/10.1088/1748-9326/ac1293>, 2021.
- 847 62. O'Neill, B. C., Tebaldi, C., van Vuuren, D. P., Eyring, V., Friedlingstein, P., Hurtt, G.,  
848 Knutti, R., Kriegler, E., Lamarque, J.-F., Lowe, J., Meehl, G. A., Moss, R., Riahi, K., and  
849 Sanderson, B. M.: The Scenario Model Intercomparison Project (ScenarioMIP) for CMIP6,  
850 *Geoscientific Model Development*, 9, 3461–3482, <https://doi.org/10.5194/gmd-9-3461-2016>,  
851 2016.
- 852 63. Park, J., and Sweet, W.: Accelerated sea level rise and Florida Current transport. *Ocean*  
853 *Science*, 11, 607–615. <https://doi.org/10.5194/os-11-607-2015>, 2015.
- 854 64. Pershing A. J., Alexander M. A., Hernandez C. M., Kerr L. A., Le Bris A., Mills K. E., Nye  
855 J. A., Record N. R., Scannell H. A., Scott J. D., Sherwood G. D., and Thomas A. C.: Slow  
856 adaptation in the face of rapid warming leads to collapse of the Gulf of Maine cod fishery,  
857 *Science*, 350, 809–812, 2015.
- 858 65. Pozo Buil M., Jacox, M. G., Fiechter, J., Alexander, M.A., Bograd, S.J., Curchitser, E.N.,  
859 Edwards, C.A., Rykaczewski, R.R., and Stock, C.A.: A Dynamically Downscaled Ensemble  
860 of Future Projections for the California Current System, *Frontiers Marine Sciences*,  
861 8:612874, doi: 10.3389/fmars.2021.612874, 2021.

- 862 66. Roberts, M. J., Jackson L. C., Roberts, C.D., Meccia V., Docquier D., Koenigk T., Ortega P.,  
863 Moreno-Chamarro., E., Bellucci, A., Coward, A., Drijfhout, S., Exarchou, E., Gutjahr, O.,  
864 Hewitt, H., Iovino, D., Lohmann, K., Putrasahan, D., Schiemann, R., Seddon, J. Terray, L.,  
865 Xu, X., Zhang, Q., Chang, P., Yeager, S. G., Castruccio, F. S., Zhang, S., and Wu, L.:  
866 Sensitivity of the Atlantic Meridional Overturning Circulation to model resolution in CMIP6  
867 HighResMIP simulations and implications for future changes. *Journal of Advances in*  
868 *Modeling Earth Systems*, 12, e2019MS002014, <https://doi.org/10.1029/2019MS002014>,  
869 2020.
- 870 67. Ross, A. C., Stock, C. A., Adcroft, A., Curchitser, E., Hallberg, R., Harrison, M. J.,  
871 Hedstrom, K., Zadeh, N., Alexander, M., Chen, W., Drenkard, E. J., du Pontavice, H.,  
872 Dussin, R., Gomez, F., John, J. G., Kang, D., Lavoie, D., Resplandy, L., Roobaert, A., Saba,  
873 V., Shin, S.-I., Siedlecki, S., and Simkins, J.: A high-resolution physical–biogeochemical  
874 model for marine resource applications in the northwest Atlantic (MOM6-COBALT-NWA12  
875 v1.0), *Geoscientific Model Development*, 16, 6943–6985, [https://doi.org/10.5194/gmd-16-](https://doi.org/10.5194/gmd-16-6943-2023)  
876 [6943-2023](https://doi.org/10.5194/gmd-16-6943-2023), 2023.
- 877 68. Ross, A. C., Stock, C. A., Koul, V., Delworth, T. L., Lu, F., Wittenberg, A., and Alexander,  
878 M. A.: Dynamically downscaled seasonal ocean forecasts for North American east coast  
879 ecosystems, *Ocean Science*, 20, 1631–1656, <https://doi.org/10.5194/os-20-1631-2024>, 2024.
- 880 69. Rutherford, K., Fennel, K., Garcia Suarez, L., and John, J. G.: Uncertainty in the evolution of  
881 northwestern North Atlantic circulation leads to diverging biogeochemical projections,  
882 *Biogeosciences*, 21, 301–314, <https://doi.org/10.5194/bg-21-301-2024>, 2024.
- 883 70. Saba, V. S., Griffies, S. M., Anderson, W. G., Winton, M., Alexander, M. A., Delworth, T.  
884 L., Hare J.A., Harrison M. J., Rosati A., Vecchi G. A., and Zhang, R.: Enhanced warming of

885 the Northwest Atlantic Ocean under climate change, *Journal of Geophysical Research:*  
886 *Oceans*, 121, 118-132, 2016.

887 71. Sanchez-Franks, A., and Zhang, J.: Decadal variability and shifts of the Gulf Stream path,  
888 *Journal of Climate*, 28, 9825-9838, 2015.

889 72. Seidov, D., Gilman, C., and Haupt, B. J.: Global Ocean Circulation: A Review of the Current  
890 State of Knowledge, *Atmosphere*, 10, 446, 2019.

891 73. Sentman, L. T., Dunne, J. P., Horowitz, L. W., Naik, V., Paulot, F., Ginoux, P., and Zadeh,  
892 N.: Quantifying equilibrium climate sensitivity to atmospheric chemistry and composition  
893 representations in GFDL-CM4.0 and GFDL-ESM4.1., *Geophysical Research Letters*,  
894 53,e2025GL116545. <https://doi.org/10.1029/2025GL116545>, 2026

895 74. Shevliakova, E., Malyshev, S., Martinez-Cano, I., Milly, P. C. D., Pacala, S. W., Ginoux, P.,  
896 Dunne, K. A., Dunne, J. P., Dupuis, C., Findell, K. L., Ghannam, K., Horowitz, L. W.,  
897 Knutson, T. R., Krasting, J. P., Naik, V., Phillipps, P., Zadeh, N., Yu, Y., Zeng, F., and  
898 Zeng, Y.: The land component LM4.1 of the GFDL Earth System Model ESM4.1: Model  
899 description and characteristics of land surface climate and carbon cycling in the historical  
900 simulation, *Journal of Advances in Modeling Earth Systems*, 16, e2023MS003922.  
901 <https://doi.org/10.1029/2023MS003922>, 2024.

902 75. Shin, S., and Alexander, M. A.: Dynamical Downscaling of Future Hydrographic Changes  
903 over the Northwest Atlantic Ocean, *Journal of Climate*, 33, 2871–2890,  
904 <https://doi.org/10.1175/JCLI-D-19-0483.1>, 2020.

905 76. Steinberg, J. M., Griffies, S. M., Krasting, J. P., Piecuch, C. G., and Ross, A. C.: A Link  
906 between U.S. East coast sea level and North Atlantic subtropical ocean heat content, *Journal*

907 of Geophysical Research:Oceans, 129, e2024JC021425.  
908 <https://doi.org/10.1029/2024JC021425>, 2024.

909 77. Stock, C. A., Dunne, J. P., Fan, S., Ginoux, P., John, J., Krasting, J. P., Laufkötter, C.,  
910 Paulot, F., and Zadeh, N.: Ocean Biogeochemistry in GFDL's Earth System Model 4.1 and  
911 Its Response to Increasing Atmospheric CO<sub>2</sub>, *J. Adv. Model. Earth Sy.*, 12,  
912 e2019MS002043, <https://doi.org/10.1029/2019MS002043>, 2020.

913 78. Stock, C. A., Dunne, J. P., Luo, J. Y., Ross, A. C., Van Oostende, N., Zadeh, N., Cordero, T.  
914 J., Liu, X., Teng Y-C.: Photoacclimation and photoadaptation sensitivity in a global ocean  
915 ecosystem model, *Journal of Advances in Modeling Earth Systems*, 17, e2024MS004701.  
916 <https://doi.org/10.1029/2024MS004701>, 2025.

917 79. Tanaka, K. R., Torre, M. P., Saba, V. S., Stock, C. A., and Chen, Y.: An ensemble high-  
918 resolution projection of changes in the future habitat of American lobster and sea scallop in  
919 the Northeast US continental shelf, *Diversity and Distributions*, 26, 987–1001,  
920 <https://doi.org/10.1111/ddi.13069>, 2020.

921 80. Volkov, D. L., Lee, S.-K., Domingues, R., Zhang, H., and Goes, M.: Interannual sea level  
922 variability along the southeastern seaboard of the United States in relation to whom it may  
923 concern: The gyre-scale heat divergence in the North Atlantic, *Geophysical Research Letters*,  
924 46, 7481–7490. <https://doi.org/10.1029/2019GL083596>, 2019.

925 81. Volkov, D.L., Smith, R.H., Garcia, R.F., Smeed, D. A., Moat, B. I, Johns, W. E., and  
926 Baringer, M. O.: Florida Current transport observations reveal four decades of steady state,  
927 *Nature Communications*, 15, 7780, <https://doi.org/10.1038/s41467-024-51879-5>, 2024.

928 82. Volkov, D.L., Zhang, K., Johns, W.E. Willis, J. K., Hobbs, W., Goes, M., Zhang, H., and  
929 Menemenlis, D.: Atlantic meridional overturning circulation increases flood risk along the

- 930 United States southeast coast, *Nature Communications*, 14, 5095,  
931 <https://doi.org/10.1038/s41467-023-40848-z>, 2023.
- 932 83. Wang, Z., Boyer, T., Reagan, J., and Hogan, P.: Upper-Oceanic Warming in the Gulf of  
933 Mexico between 1950 and 2020, *Journal of Climate*, 36, 2721–2734,  
934 <https://doi.org/10.1175/JCLI-D-22-0409.1>, 2023.
- 935 84. Wang, Z. A., Wanninkhof, R., Cai, W.-J., Byrne, R. H., Hu, X., Peng, T.-H., and Huang, W.-  
936 J.: The marine inorganic carbon system along the Gulf of Mexico and Atlantic coasts of the  
937 United States: Insights from a transregional coastal carbon study, *Limnology and*  
938 *Oceanography*, 58, 325–342, 2013.
- 939 85. Wanninkhof, R., Barbero, L., Byrne, R., Cai, W.-J., Zhang, H. Z., Baringer, M., and  
940 Langdon, C.: Ocean acidification along the Gulf Coast and East Coast of the USA,  
941 *Continental Shelf Research*, 98, 54–71. 2015.
- 942 86. Weijer, W., Cheng, W., Garuba, O. A., Hu, A., and Nadiga, B. T.: CMIP6 models predict  
943 significant 21st century decline of the Atlantic Meridional Overturning Circulation,  
944 *Geophysical Research Letters*, 47, e2019GL086075. <https://doi.org/10.1029/2019GL086075>,  
945 2020.
- 946 87. Weinberg, J. R.: Bathymetric shift in the distribution of Atlantic surfclams: response to  
947 warmer ocean temperature, *ICES Journal of Marine Science*, 62, 1444–1453,  
948 <https://doi.org/10.1016/j.icesjms.2005.04.020>, 2005.
- 949 88. Worthington, L. V.: On the north Atlantic circulation, *John Hopkins Oceanographic Studies*,  
950 6, 110, 1976.

- 951 89. Yang, J., and Chen, K.: Profound changes in the seasonal cycle of sea level along the United  
952 States Mid-Atlantic Coast. *Geophysical Research Letters*, 52, e2024GL112273.  
953 <https://doi.org/10.1029/2024GL112273>, 2025.
- 954 90. Yin, J., Schlesinger, M. and Stouffer, R.: Model projections of rapid sea-level rise on the  
955 northeast coast of the United States. *Nature Geosciences*, 2, 262–266,  
956 <https://doi.org/10.1038/ngeo462>, 2009.
- 957 91. Yuan, Y., Castelao, R.M. and He, R.: Variability in along-shelf and cross-shelf circulation in  
958 the South Atlantic Bight, *Continental Shelf Research*, 134, 52-62,  
959 <https://doi.org/10.1016/j.csr.2017.01.006>, 2017.
- 960 92. Zantopp, R., Fischer, J., Visbeck, M., and Karstensen, J.: From interannual to decadal: 17  
961 years of boundary current transports at the exit of the Labrador Sea, *Journal of Geophysical*  
962 *Research: Oceans*, 122, 1724–1748, doi:10.1002/2016JC012271, 2017.
- 963 93. Zhang, W., Alatalo, P., Crockford, T., Hirzel, A.J., Meyer, M.G., Oliver, H., Peacock, E.,  
964 Petitpas, C.M., Sandwith, Z., Smith, W.O., Sosik, H.M., Stanley, R.H.R., Stevens, B.L.F.,  
965 Turner, J.T., and McGillicuddy, D.J.: Cross-shelf exchange associated with a shelf-water  
966 streamer at the Mid-Atlantic Bight shelf edge. *Progress in Oceanography*, 210, 102931, 2023.
- 967 94. Zhao, M., Golaz, J.-C., Held, I. M., Guo, H., Balaji, V., Benson, R., Chen, J. H., Chen, X.,  
968 Donner, L. J., Dunne, J., Dunne, K. A., Durachta, J., Fan, S.-M., Freidenreich, S. M., Garner,  
969 S. T., Ginoux, P., Harris, L., Horowitz, L. W., Krasting, J. P., Langenhorst, A. R., Zhi, L.,  
970 Lin, P., Lin, S. J., Malyshev, S., Mason, E., Milly, P. C. D., Ming, Y., Naik, V., Paulot, F.,  
971 Paynter, D., Phillipps, P. J., Radhakrishnan, A., Ramaswamy, V., Robinson, T.,  
972 Schwarzkopf, D., Seman, C. J., Shevliakova, E., Shen, Z., Shin, H. H., Silvers, L. G., Wilson,  
973 J. R., Winton, M., Wittenberg, A. T., Wyman, B., and Xiang, B.: The GFDL Global

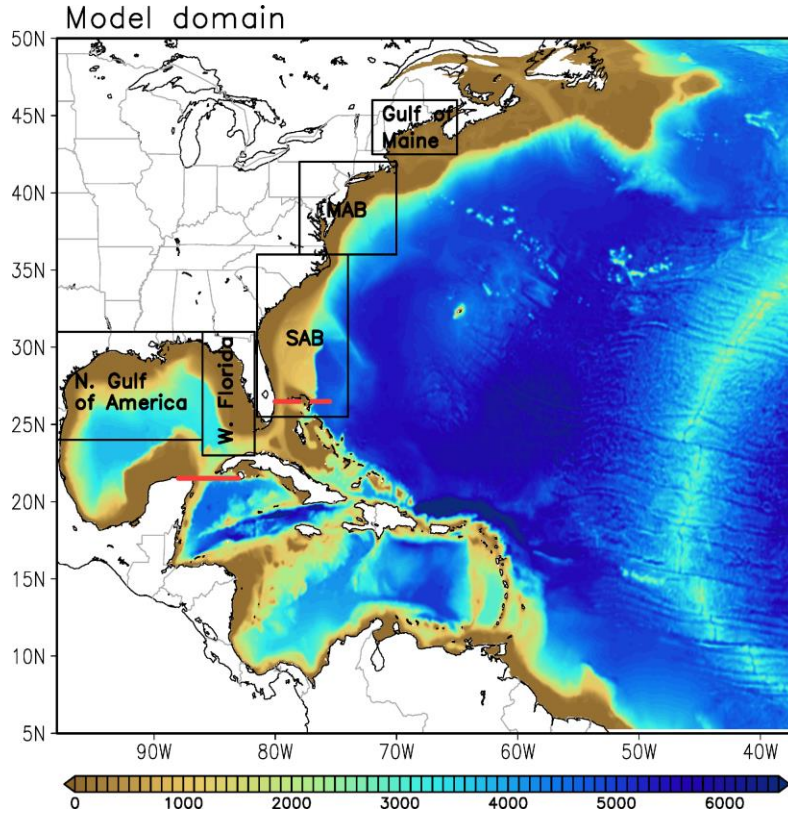
974 Atmosphere and Land Model AM4.0/LM4.0: 1. Simulation characteristics with prescribed  
975 SSTs, *Journal of Advances in Modeling Earth Systems*, 10, 691–734,  
976 <https://doi.org/10.1002/2017ms001208>, 2018.

977 95. Zhao, M., Golaz, J. C., Held, I. M., Guo, H., Balaji, V., Benson, R., Chen, J. H., Chen, X.,  
978 Donner, L. J., Dunne, J. P., Dunne, K., Durachta, J., Fan, S. M., Freidenreich, S. M., Garner,  
979 S. T., Ginoux, P., Harris, L. M., Horowitz, L. W., Krasting, J. P., Langenhorst, A. R., Liang,  
980 Z., Lin, P., Lin, S. J., Malyshev, S. L., Mason, E., Milly, P. C. D., Ming, Y., Naik, V., Paulot,  
981 F., Paynter, D., Phillipps, P., Radhakrishnan, A., Ramaswamy, V., Robinson, T.,  
982 Schwarzkopf, D., Seman, C. J., Shevliakova, E., Shen, Z., Shin, H., Silvers, L. G., Wilson, J.  
983 R., Winton, M., Wittenberg, A. T., Wyman, B., and Xiang, B.: The GFDL Global  
984 Atmosphere and Land Model AM4.0/LM4.0: 2. Model Description, Sensitivity Studies, and  
985 Tuning Strategies, *Journal of Advances in Modeling Earth Systems*, 10, 735–769,  
986 <https://doi.org/10.1002/2017MS001209>, 2018.

987

988 Figure list

989



990

991 **Fig. 1.** MOM6-NWA12 model domain and bathymetry (m). The black boxes indicate the  
992 location of the Northern Gulf of America, West Florida, South Atlantic Bight (SAB), and middle  
993 Atlantic Bight (MAB), and Gulf of Maine for exploring sea-level rise. The red solid lines are the  
994 locations of four major Northwestern Atlantic boundary current systems (Yucatan Current,  
995 Florida Current, Antilles Current (0~500 m), and Deep Western Boundary Current (1,000-  
996 4,000m).

997

998

999

1000

1001

1002

1003

1004

1005

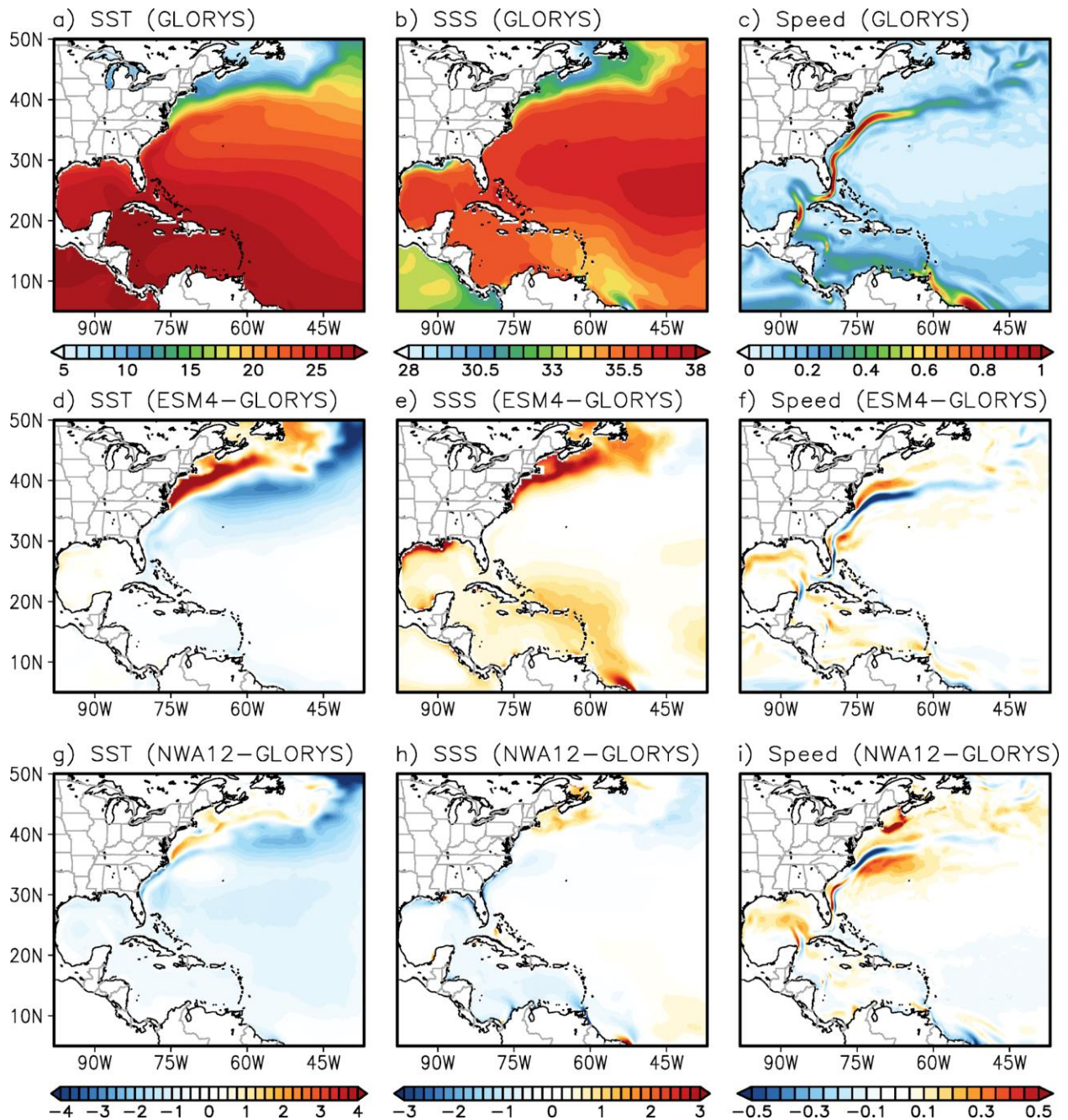
1006

1007

1008

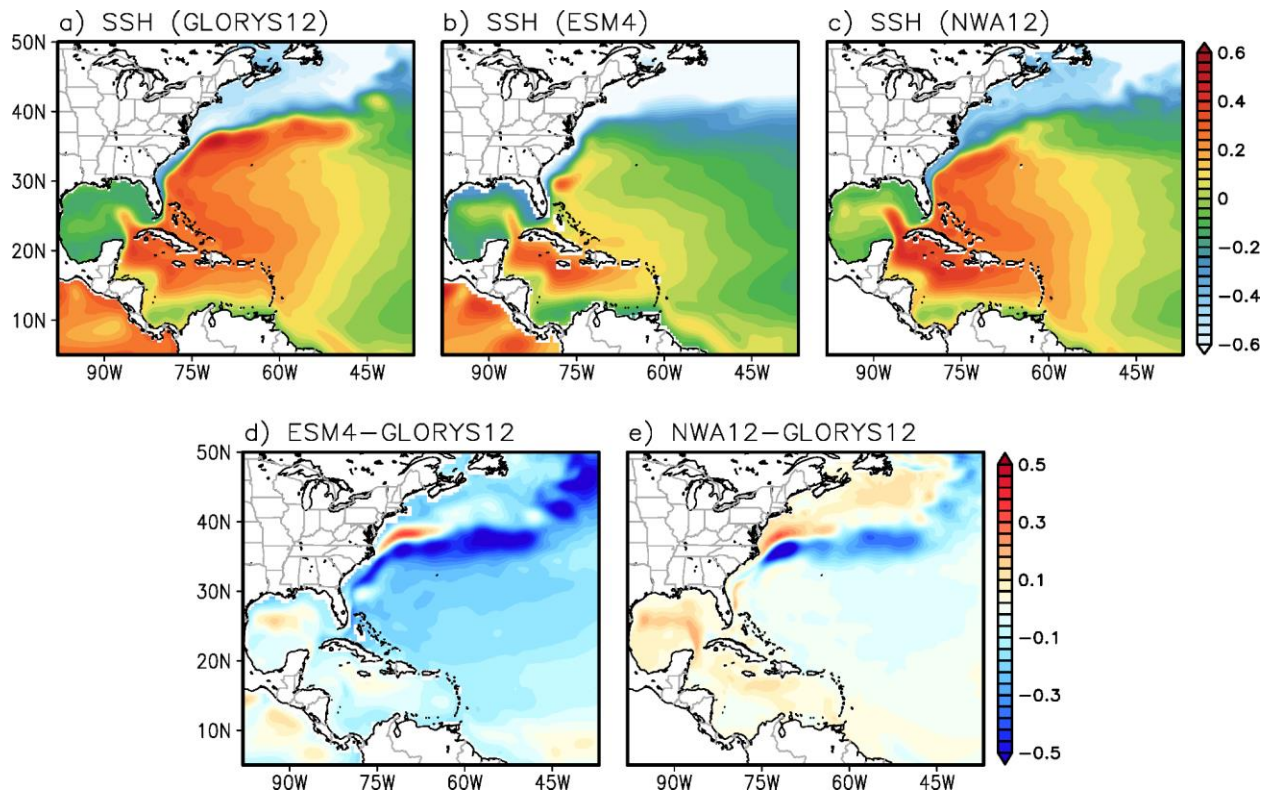
1009

1010



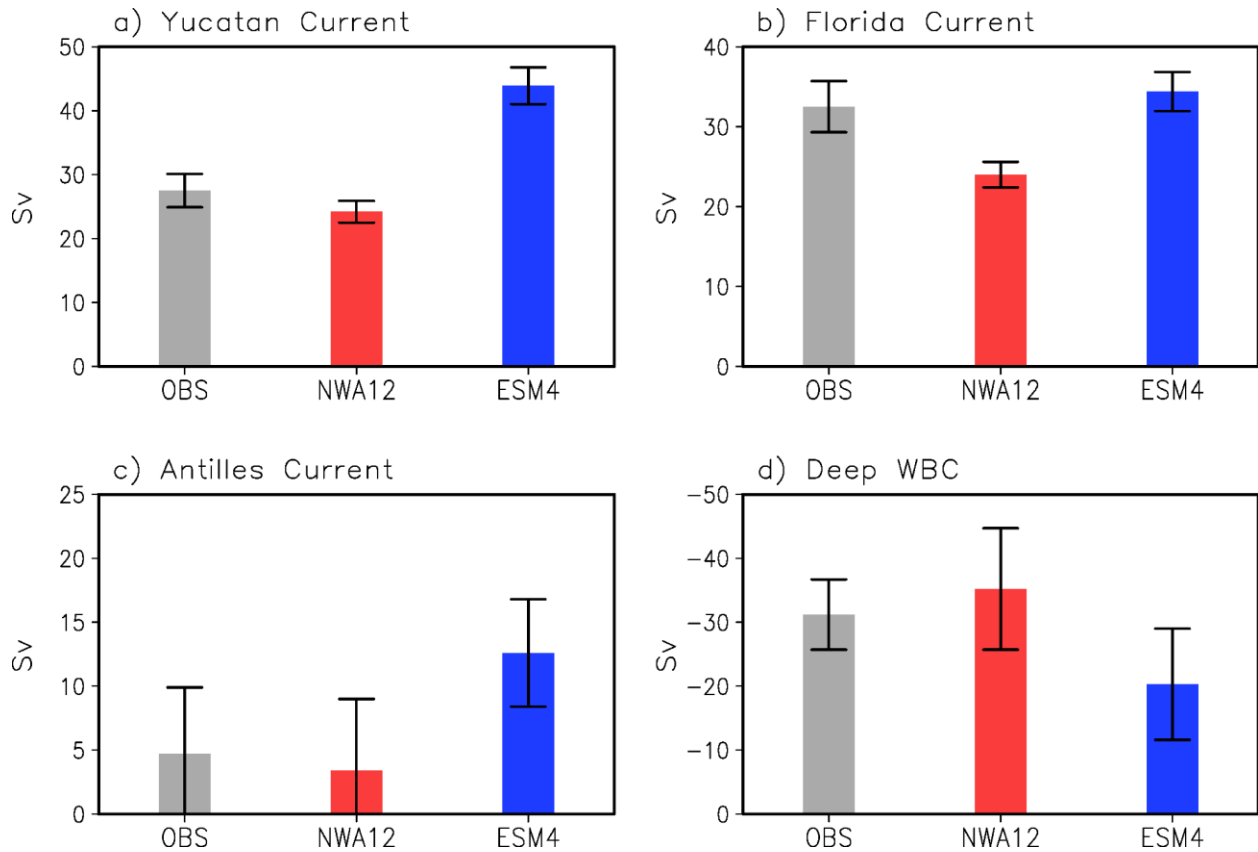
1011  
 1012 **Fig. 2.** Spatial patterns of the historical (1993–2020) mean (a) sea surface temperature (SST, °C),  
 1013 (b) sea surface salinity (SSS, psu), and (c) surface current speed ( $\text{m s}^{-1}$ ) in GLORYS12. (d)–(f)  
 1014 show the GFDL-ESM4 biases for SST, SSS, and surface current speed. (g)–(i) are the same as  
 1015 (d)–(f), but for MOM6-NWA12.

1016  
 1017  
 1018  
 1019  
 1020



1021  
 1022  
 1023  
 1024  
 1025  
 1026  
 1027  
 1028

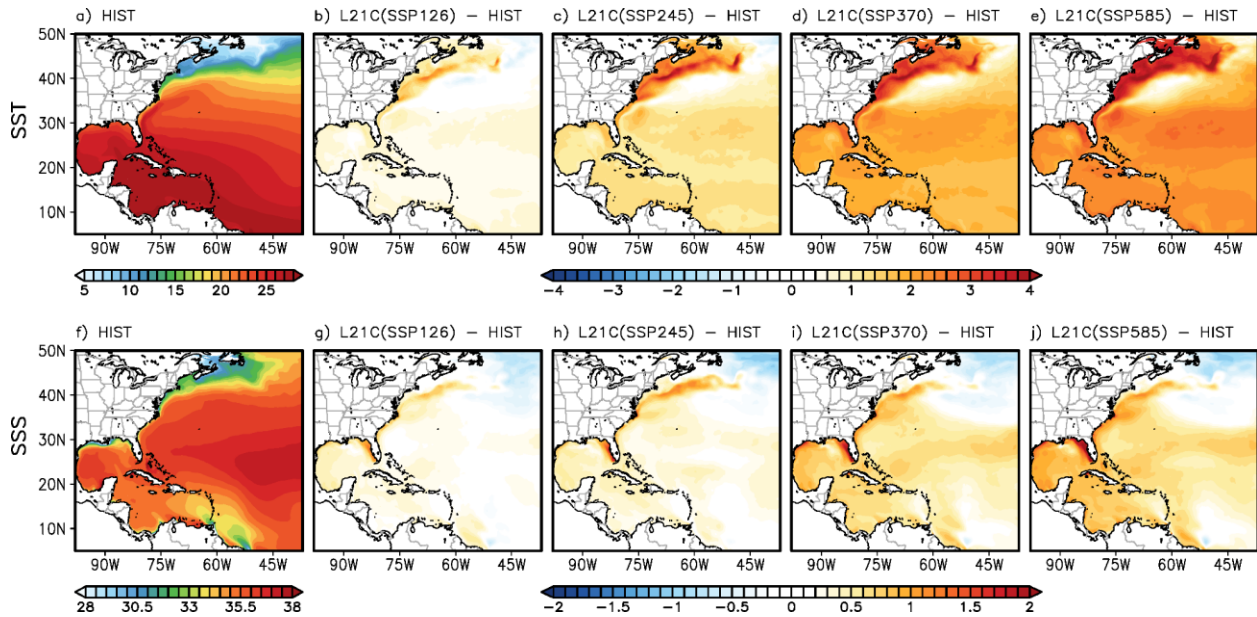
**Fig. 3.** Spatial pattern of the historical (1993-2020) mean sea surface height (SSH, m) in (a) GLORYS12, (b) GFDL-ESM4.1 and (c) MOM6-NWA12. (d) The difference between GFDL-ESM4.1 and GLORYS12. (e) difference between MOM6-NWA12 and GLORYS12.



1029  
1030

1031 **Fig. 4.** The historical mean (1993-2020) of (a) the Yucatan Channel, (b) Florida Current, (c)  
1032 Antilles Current, and (d) Deep Western Boundary Current transport derived from observational  
1033 records (gray bars), MOM6-NWA12 (red bars) and GFDL-ESM4 (blue bars). Note that the  
1034 observational transport records of the Florida Current, Yucatan Current, Antilles Current, and  
1035 Deep Western Boundary Current (DWBC) are from Volkov et al. (2024), Athié et al. (2020),  
1036 Meinen et al. (2019) and Zantopp et al. (2017), respectively.

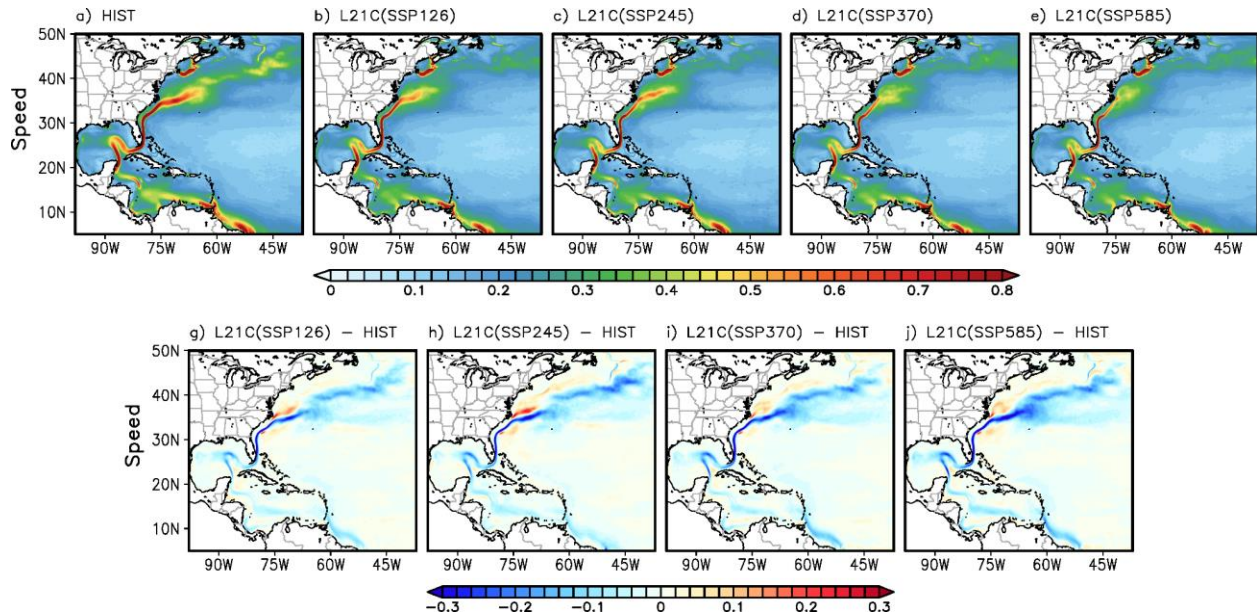
1037  
1038  
1039  
1040  
1041  
1042  
1043  
1044  
1045  
1046  
1047  
1048



1049 **Fig. 5.** (a) Spatial patterns of sea surface temperature (SST, °C) derived from MOM6-NWA12  
 1050 during (a) historical period (1993-2020). The differences in SST between the future (2073-2100)  
 1051 and historical periods in the (b) SSP-126, (c) SSP-245, (d) SSP-370 and (e) SSP-585 simulations.  
 1052 (f)-(j) are the same (a)-(e) but for sea surface salinity (SSS, psu).  
 1053

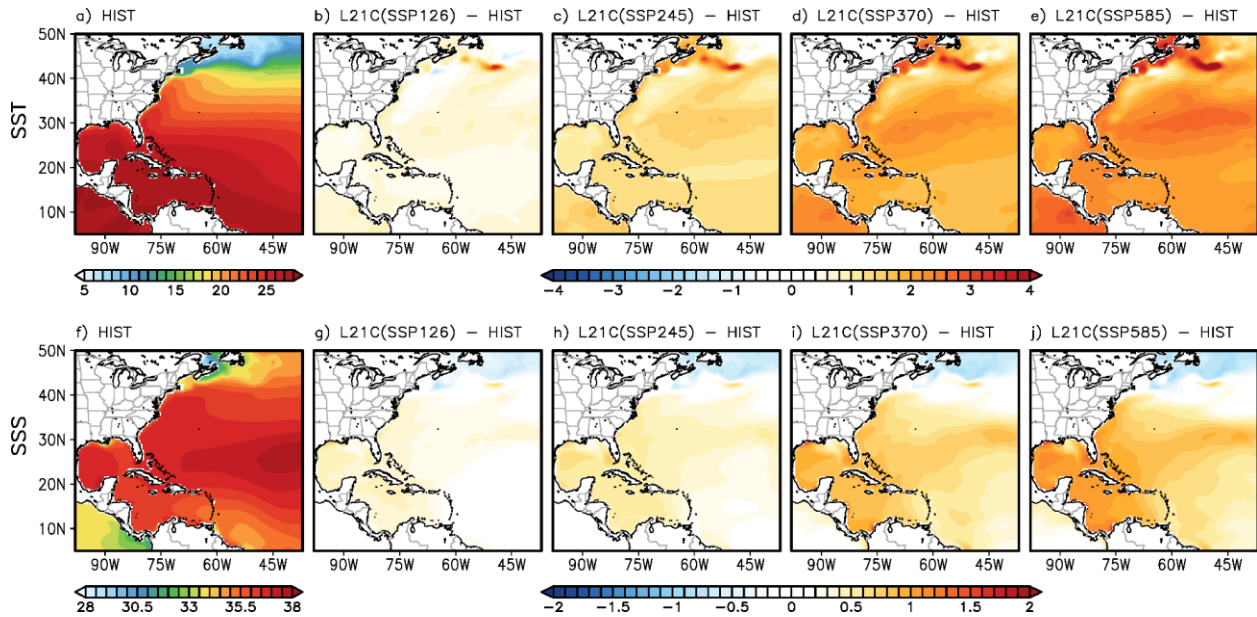
1054  
 1055  
 1056  
 1057  
 1058

1059  
1060  
1061  
1062  
1063  
1064  
1065



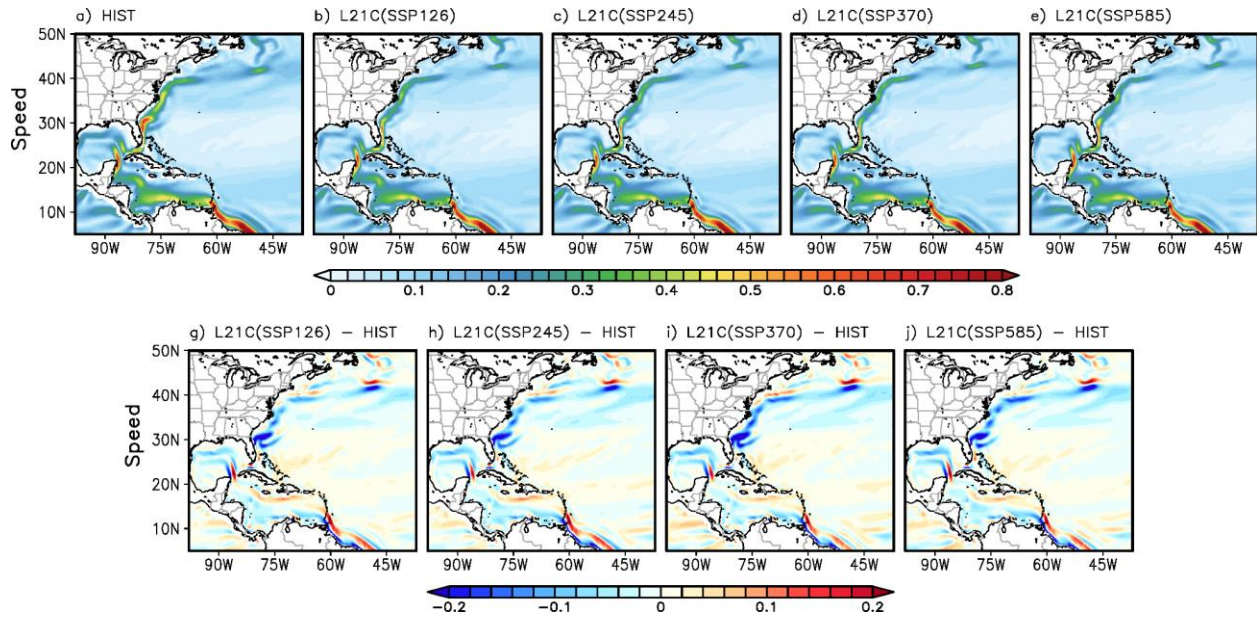
1066  
1067  
1068  
1069  
1070  
1071  
1072  
1073  
1074  
1075

**Fig. 6.** Spatial surface current speed ( $\text{m s}^{-1}$ ) patterns derived from MOM6-NWA12 during (a) the historical (1993-2020) period and future (2073-2100) period in (b) SSP-126, (c) SSP-245, (d) SSP-370 and (e) SSP585 simulations. The difference in surface current speed between the future and historical periods in (g) SSP-126, (h) SSP-245, (i) SSP-370 and (j) SSP585 simulations, respectively.



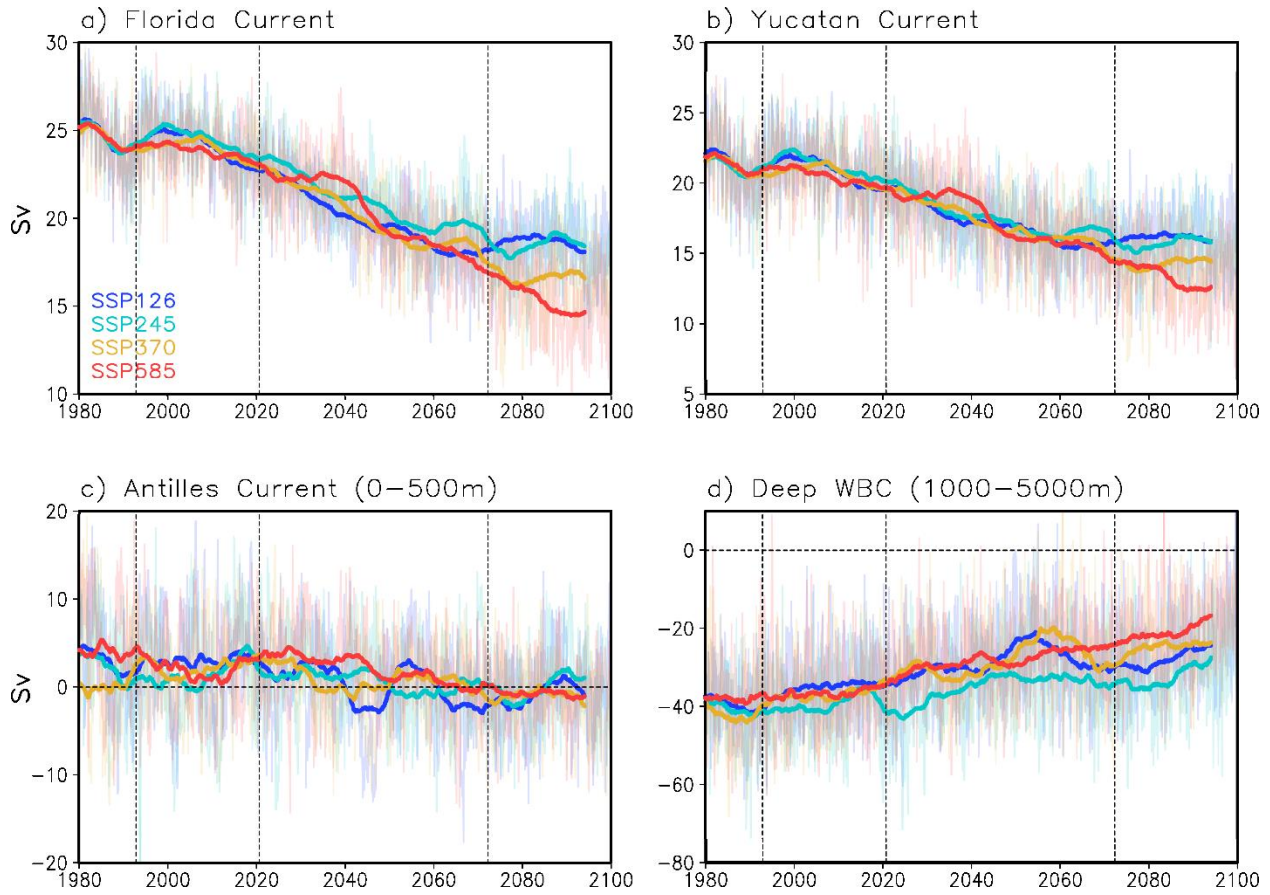
1076  
 1077  
 1078  
 1079  
 1080  
 1081  
 1082  
 1083

**Fig. 7.** (a) Spatial patterns of sea surface temperature (SST) derived from GFDL-ESM4.1 during the historical period (1993-2020). (b)-(e) are the differences in SST between the future (2073-2100) and historical (1993-2020) periods in the SSP-126, SSP-245, SSP-370, and SSP-585 simulations, respectively. (f) and (j) are the same (a) and (e) but for the sea surface salinity (SSS).



1084  
 1085  
 1086  
 1087  
 1088  
 1089  
 1090  
 1091  
 1092

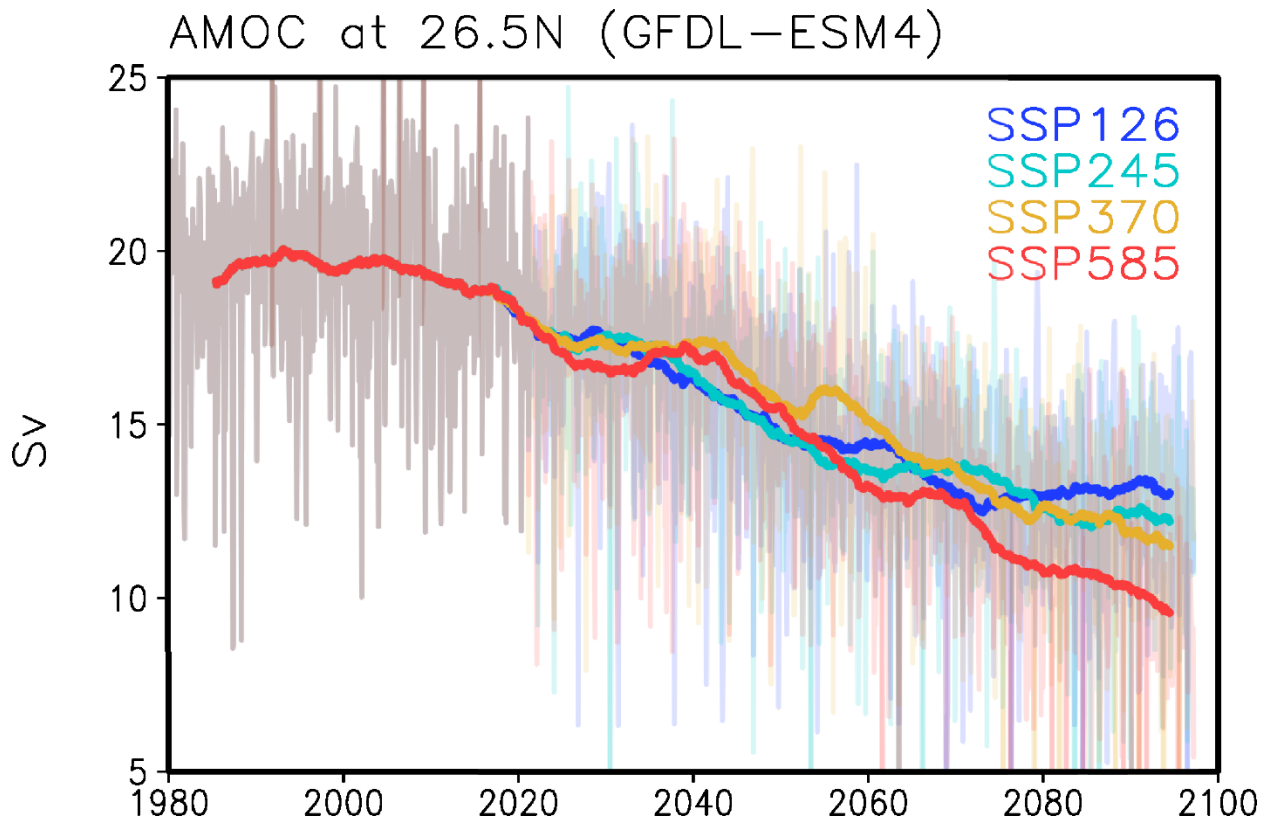
**Fig. 8.** Spatial surface current speed patterns derived from GFDL-ESM4.1 during (a) the historical (1993-2020) period, and future (2073-2100) period in the (b) SSP-126, (c) SSP-245, (d) SSP-370, and (e) SSP-585 simulations. The difference in surface current speed between the future and historical periods in (g) SSP-126, (h) SSP-245, (i) SSP-370, and (j) SSP-585 simulations, respectively.



1093  
 1094 **Fig. 9.** Time series of (a) the Florida Current transport, (b) transport across the Yucatan Channel,  
 1095 (c) Antilles Current transport and (d) Deep Western Boundary Current transport in MOM6-  
 1096 NWA12. The cyan, green, orange, and red lines are the SSP-126, SSP-245, SSP-370 and SSP-  
 1097 585 simulations, respectively. The bold lines indicate 11-year running means. The dotted lines  
 1098 indicate the historical and future periods. The vertical dotted lines indicate the historical and  
 1099 future averaging periods.

1100  
 1101  
 1102  
 1103  
 1104  
 1105  
 1106  
 1107  
 1108  
 1109  
 1110  
 1111  
 1112  
 1113  
 1114

1115



1116

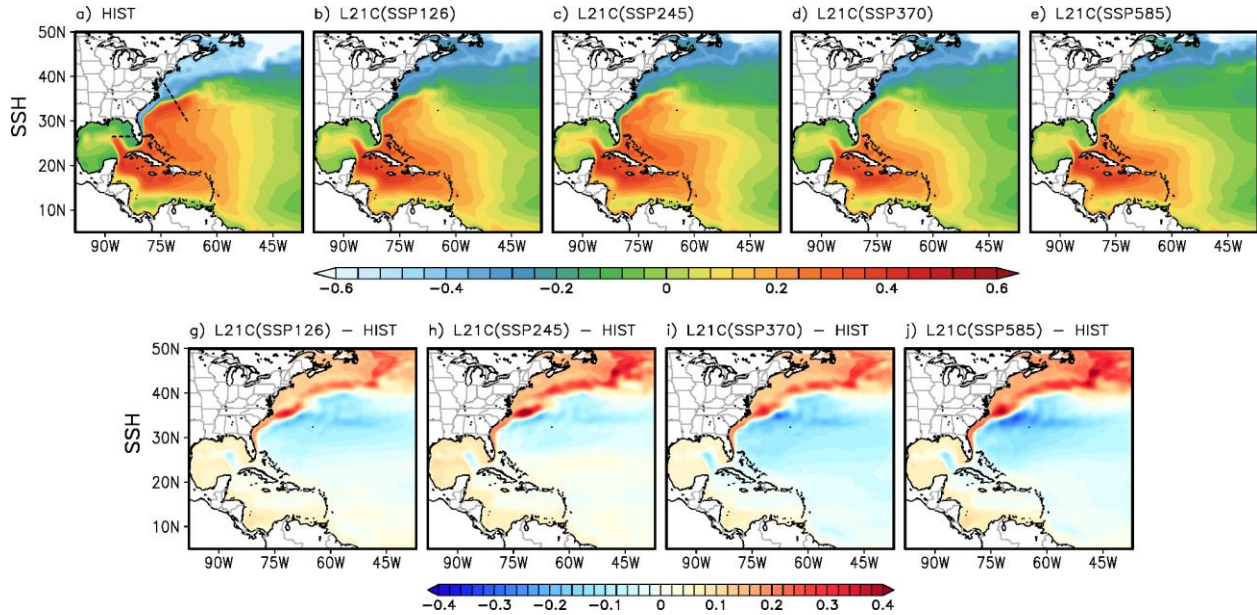
1117

1118

1119

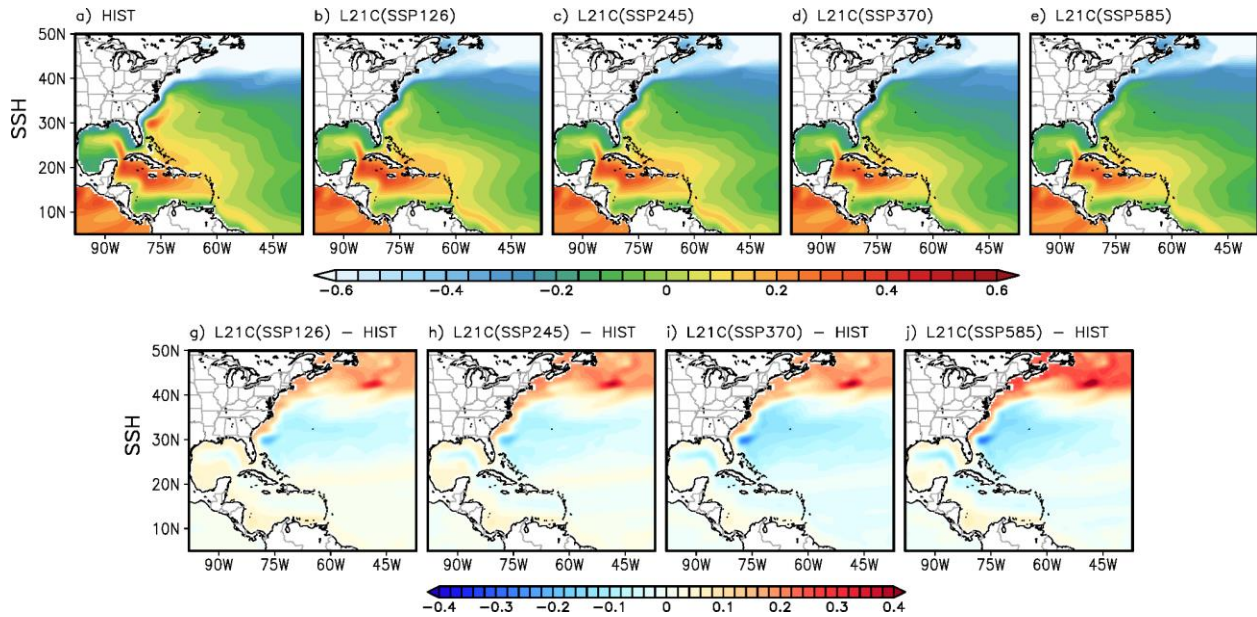
**Fig. 10.** Time series of AMOC in GFDL-ESM4.1. The blue, green, orange, and red lines are the SSP-126, SSP-245, SSP-370 and SSP-585 simulations, respectively.

1120  
1121



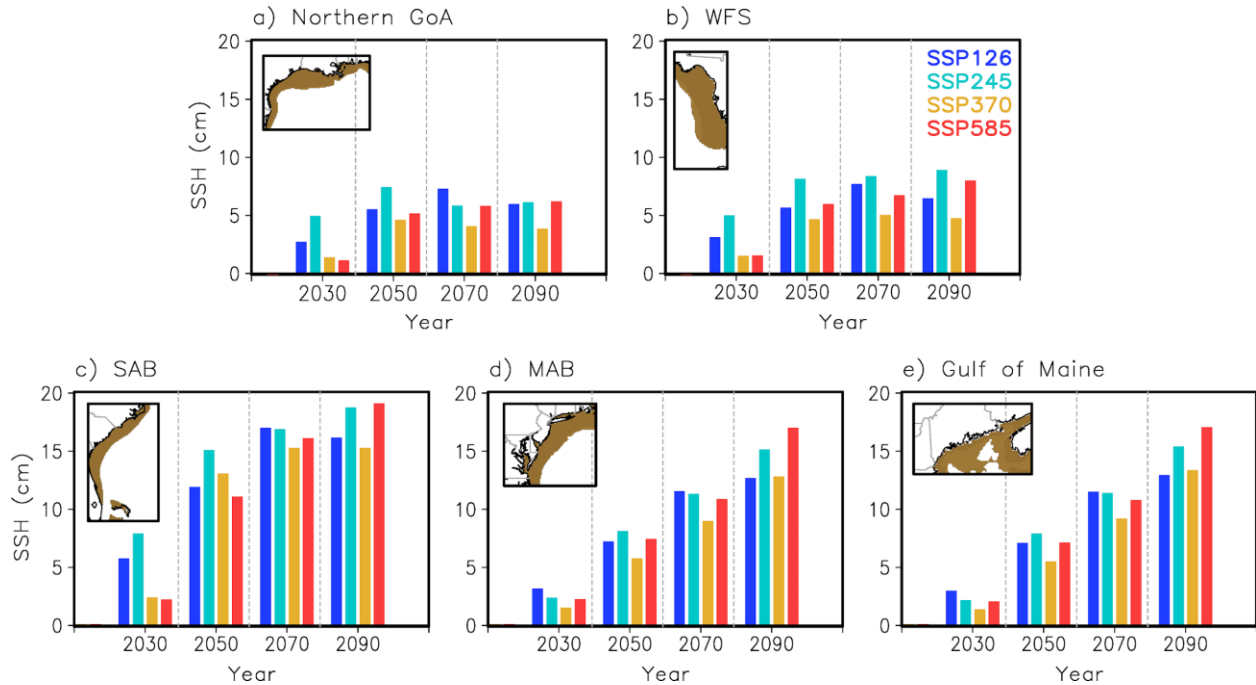
1122  
1123  
1124  
1125  
1126  
1127  
1128  
1129  
1130  
1131  
1132  
1133

**Fig. 11.** Spatial sea surface height (SSH, m) patterns derived from MOM6-NWA12 during (a) the historical (1993-2020) period, and future (2073-2100) period from (b) SSP-126, (c) SSP-245, (d) SSP-370 and (e) SSP-585 simulations. The difference in SSH between the future and historical periods from (g) SSP-126, (h) SSP-245, (i) SSP-370, and (j) SSP-585 simulations, respectively. The black dotted lines in (a) indicate the locations of vertical cross-section in Fig.15-17.



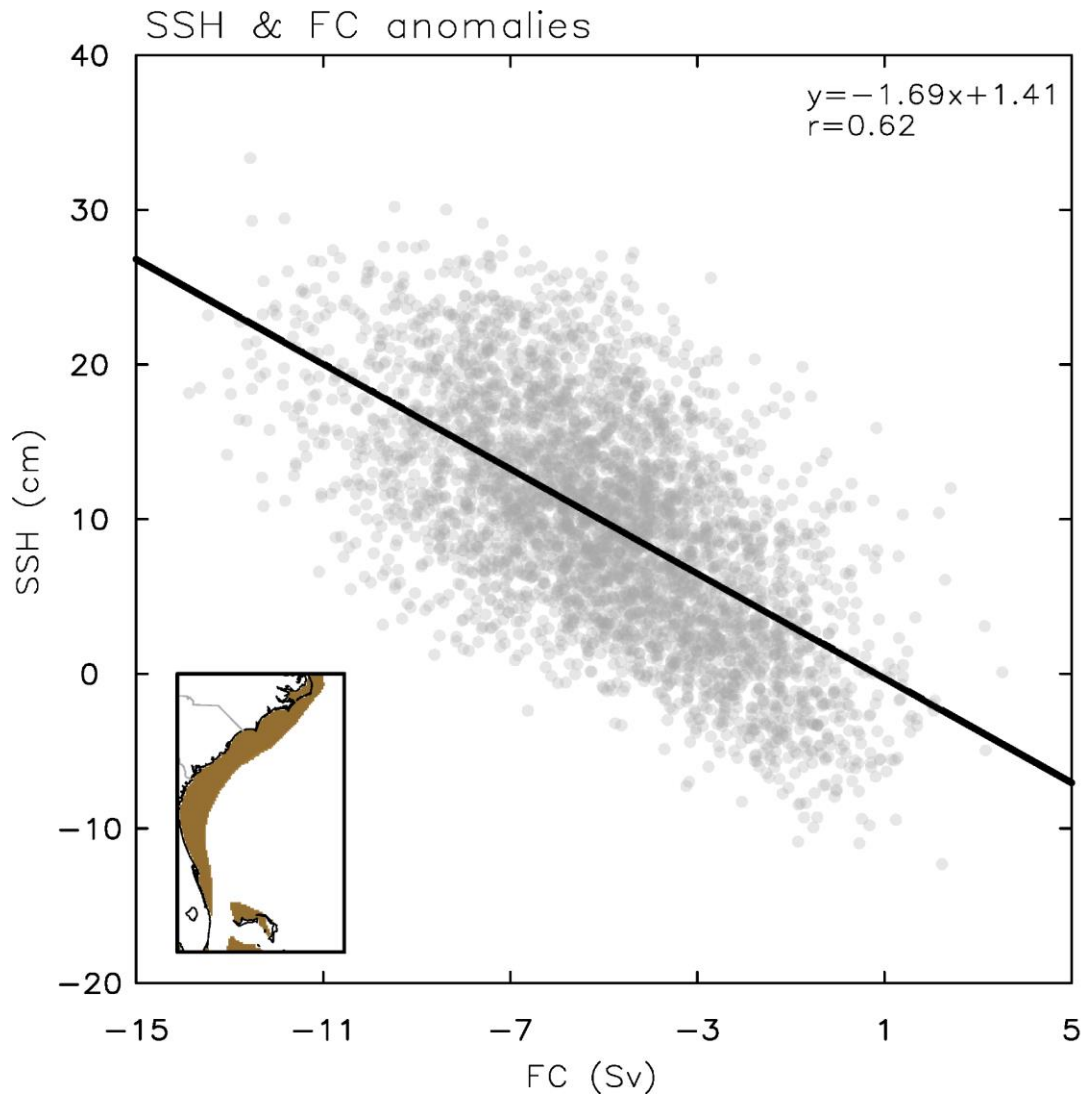
1134  
 1135 **Fig. 12.** Spatial SSH patterns derived from GFDL-ESM4.1 during (a) the historical (1993-2020)  
 1136 period, and future (2073-2100) period from (b) SSP-126, (c) SSP-245, (d) SSP-370, and (e) SSP-  
 1137 585 simulations, respectively. The difference in SSH between the future and historical periods  
 1138 from (g) SSP-126, (h) SSP-245, (i) SSP-370 and (j) SSP-585 simulations, respectively.

1139  
 1140  
 1141  
 1142  
 1143  
 1144  
 1145  
 1146  
 1147  
 1148  
 1149  
 1150  
 1151  
 1152  
 1153  
 1154  
 1155  
 1156



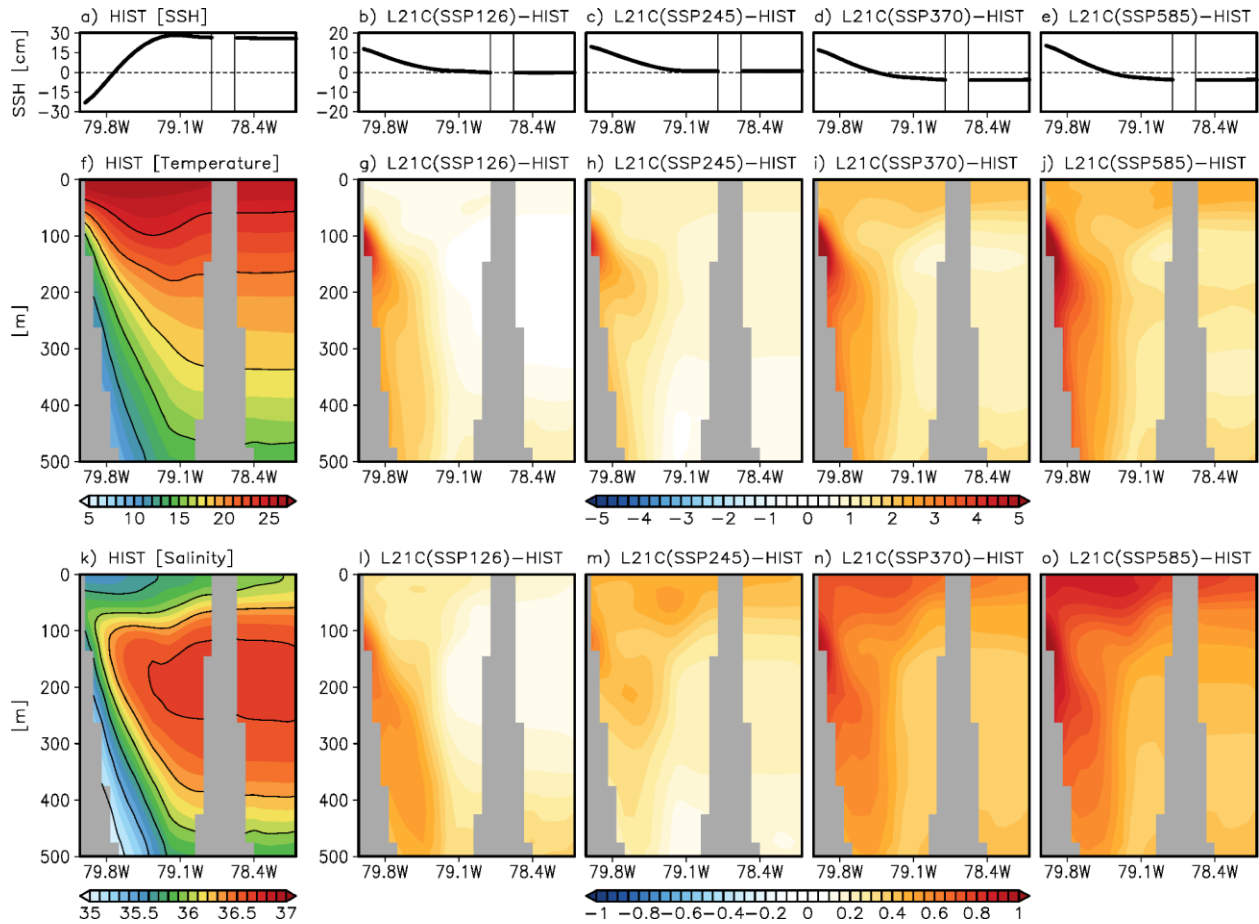
1157  
 1158 **Fig. 13.** Spatially averaged sea level changes (cm) from historical period (1993-2020) in (a) the  
 1159 northern Gulf of America, (b) West Florida shelf, (c) the South Atlantic Bight, (d) the Middle  
 1160 Atlantic Bight, and (e) the Gulf of Maine under the SSP-126 (blue bars), SSP-245 (green bars),  
 1161 SSP-370 (orange bars) and SSP-585 (red bars) simulations. The dynamic sea level changes are  
 1162 spatially averaged over the shelf regions below 200 m depth (brown-colored area in the maps).  
 1163 The years on the x-axis represent the center of a 20-year averaging period (e.g., the value for  
 1164 2030 represents the average from 2021 to 2040).

1165  
 1166  
 1167  
 1168  
 1169  
 1170  
 1171  
 1172  
 1173  
 1174  
 1175  
 1176  
 1177



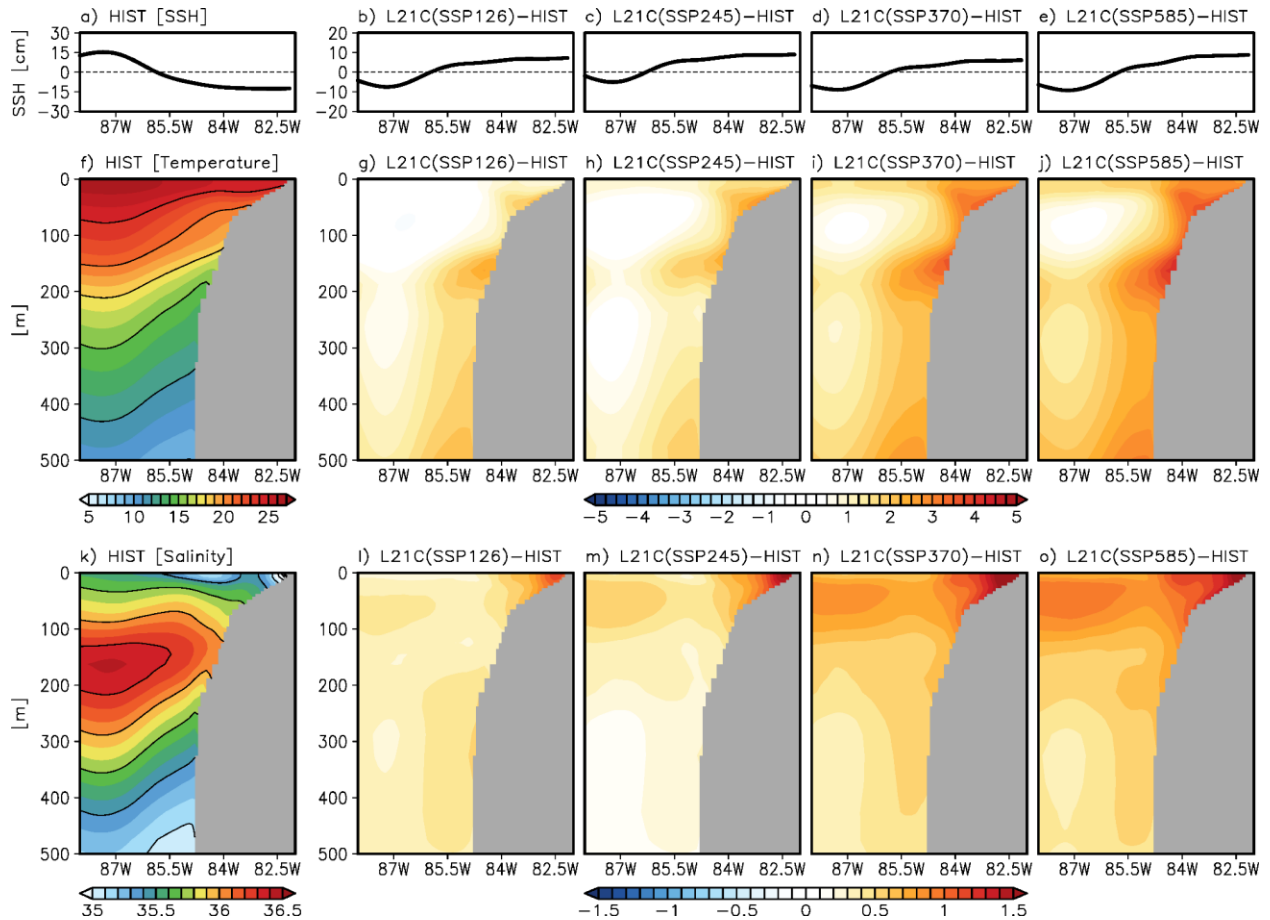
1178  
 1179  
 1180  
 1181  
 1182  
 1183  
 1184  
 1185

**Fig. 14.** Scatter plot of anomalous Florida Current (FC) transport (Sv) versus dynamic sea level (cm) change along the South Atlantic Bight derived from all four SSP simulations. The dynamic sea level change is spatially averaged over the shelf regions below 200 m (brown-colored area in the map).



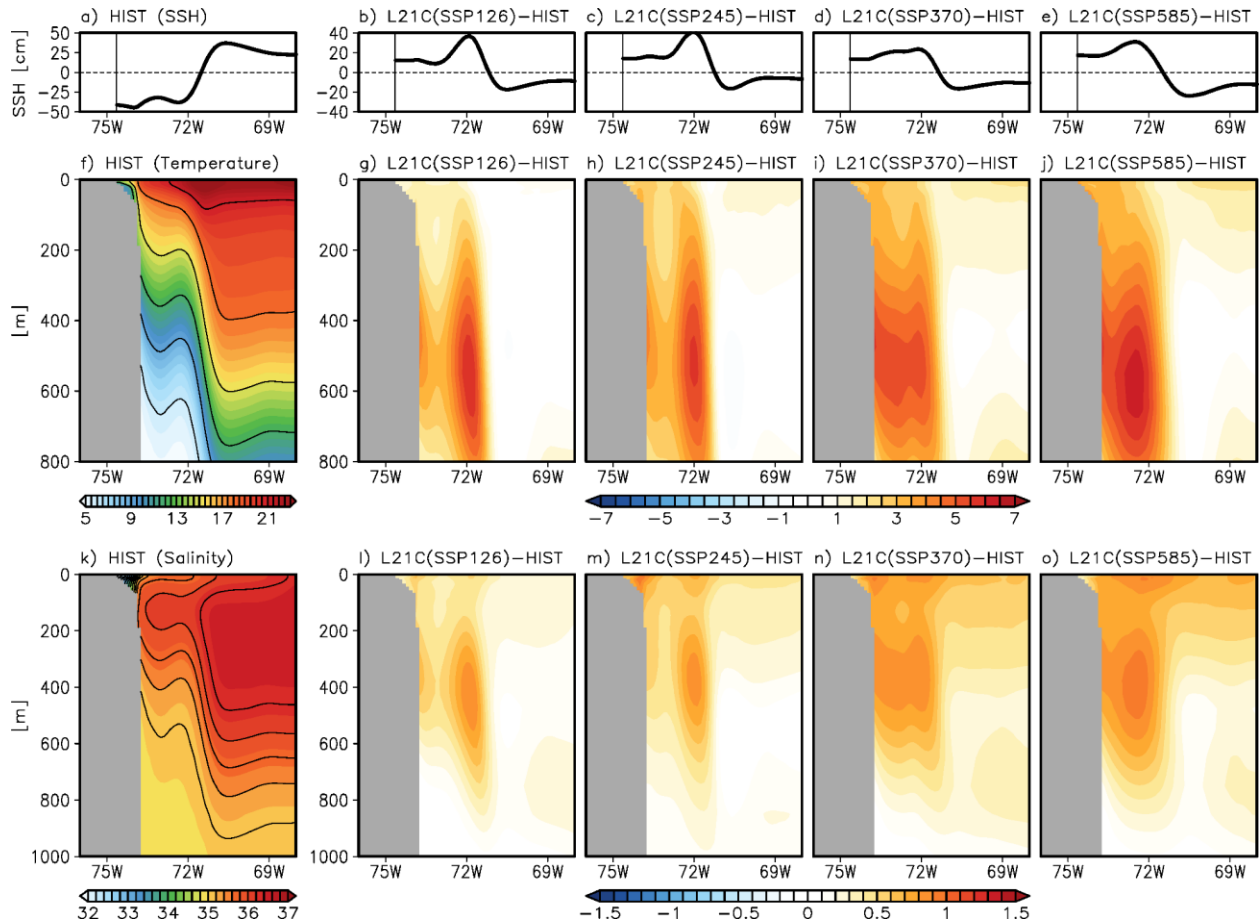
1186  
 1187  
 1188  
 1189  
 1190  
 1191  
 1192  
 1193  
 1194  
 1195  
 1196  
 1197  
 1198  
 1199  
 1200  
 1201  
 1202  
 1203  
 1204  
 1205

**Fig. 15.** (a) Sea level at the east coast of Florida ( $26.5^{\circ}\text{N}$ ,  $79.7^{\circ}\text{W}$ - $78.0^{\circ}\text{W}$ ) during the historical period. Future change in the sea level at the east coast of Florida from (b) SSP-126, (c) SSP-245, (d) SSP-370, (e) SSP-585, and (c) SSP-585 simulations. (f) The vertical cross-sections of the mean temperature across the east coast of Florida during the historical period. The difference in temperature between the future and historical periods from (g) SSP-126, (h) SSP-245, (i) SSP-370, and (j) SSP-585 simulations, respectively. (k)-(o) are the same as (f)-(j) but for salinity.



1206  
 1207  
 1208  
 1209  
 1210  
 1211  
 1212  
 1213  
 1214  
 1215  
 1216  
 1217  
 1218  
 1219  
 1220  
 1221  
 1222  
 1223  
 1224  
 1225

**Fig. 16.** (a) Sea level at West Florida ( $26.5^{\circ}\text{N}$ ,  $88^{\circ}\text{W}$ - $81^{\circ}\text{W}$ ) during the historical period. Future change in the sea level at West Florida from (b) SSP-126, (c) SSP-245, (d) SSP-370, (e) SSP-585, and (c) SSP-585 simulations. (f) The vertical cross-sections of the mean temperature ( $^{\circ}\text{C}$ ) across West Florida during the historical period. The difference in temperature between the future and historical periods from (g) SSP-126, (h) SSP-245, (i) SSP-370, and (j) SSP-585 simulations, respectively. (k)-(o) are the same as (f)-(j) but for salinity (psu).



1226  
1227  
1228  
1229  
1230  
1231  
1232  
1233

**Fig. 17.** (a) Sea level at the MAB ( $30^{\circ}\text{N}$ - $41^{\circ}\text{N}$ ,  $76^{\circ}\text{W}$ - $67^{\circ}\text{W}$ ) during the historical period. Future change in the sea level at the MAB from (b) SSP-126, (c) SSP-245, (d) SSP-370, (e) SSP-585, and (c) SSP-585 simulations. (f) The vertical cross-sections of the mean temperature ( $^{\circ}\text{C}$ ) across the MAB during the historical period. The difference in temperature between the future and historical periods from (g) SSP-126, (h) SSP-245, (i) SSP-370, and (j) SSP-585 simulations, respectively. (k)-(o) are the same as (f)-(j) but for salinity (psu).